Cell

Rapid adaptation to CDK2 inhibition exposes intrinsic cell-cycle plasticity

Graphical abstract

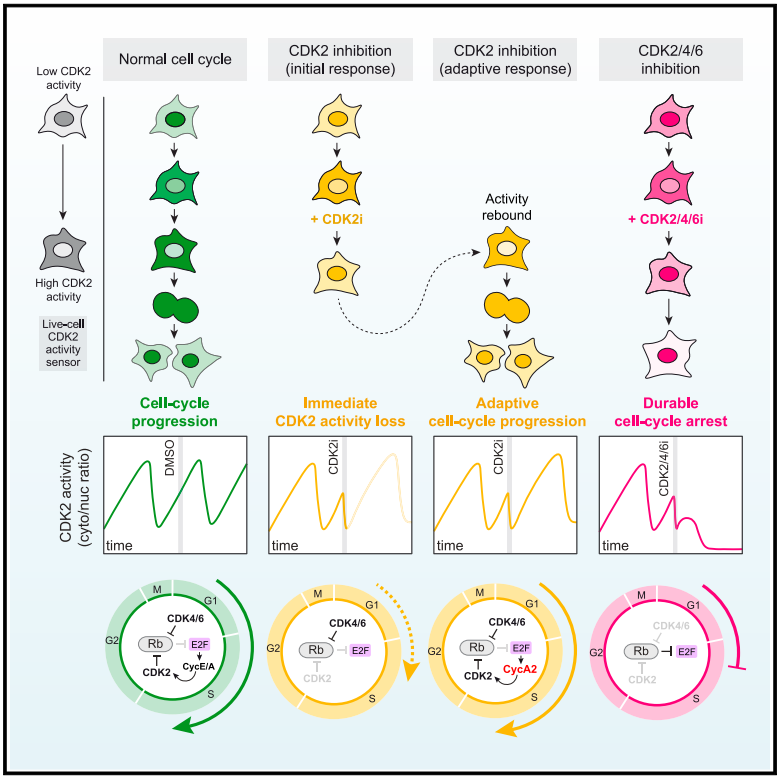

Authors

Mansi Arora, Justin Moser, Timothy E. Hoffman, ..., Mariano Barbacid, Nichol Miller, Sabrina L. Spencer

Correspondence

sabrina.spencer@colorado.edu

In brief

Selective CDK2 inhibition initially blocks substrate phosphorylation. However, because of a potent positive feedback loop and reinforcement by CDK4/6 activity, cells can rapidly overcome CDK2 inhibition to complete the cell cycle.

Highlights

- CDK2 inhibition (CDK2i) causes rapid loss of kinase activity followed by a rebound
- CDK2i unmasks CDK4/6 activity beyond G1, reinforcing Rb hyperphosphorylation
- The Rb-E2F axis remains engaged under CDK2i, driving cyclin A and CDK2 activity
- Co-inhibiting CDK2 and CDK4/6 presents a strategy to force durable cell-cycle exit

Arora et al., 2023, Cell *186*, 2628–2643
June 8, 2023
https://doi.org/10.1016/j.cell.2023.05.013

CellPress

CellPress

Cell

Article

Rapid adaptation to CDK2 inhibition exposes intrinsic cell-cycle plasticity

Mansi Arora,[1,7,14] Justin Moser,[1,8,14] Timothy E. Hoffman,[1,14] Lotte P. Watts,[1,14] Mingwei Min,[1,2] Monica Musteanu,[3,4,9] Yao Rong,[1,5] C. Ryland III,[1] Varuna Nangia,[1] Jordan Schneider,[1,10] Manuel Sanclemente,[3] John Lapek,[6,11] Lisa Nguyen,[6,12] Sherry Niessen,[6,11] Stephen Dann,[6,12] Todd VanArsdale,[6] Mariano Barbacid,[3,4] Nichol Miller,[6,13] and Sabrina L. Spencer[1,15,*]

[1]Department of Biochemistry and BioFrontiers Institute, University of Colorado-Boulder, Boulder, CO 80303, USA
[2]Guangzhou Laboratory, Guangzhou, Guangdong, China
[3]Experimental Oncology Group, Molecular Oncology Programme, Spanish National Cancer Research Centre, Madrid, Spain
[4]Centro de Investigación Biomédica en Red de Cáncer (CIBERONC), Instituto de Salud Carlos III, 28029 Madrid, Spain
[5]Department of Molecular, Cellular, and Developmental Biology and BioFrontiers Institute, University of Colorado-Boulder, Boulder, CO 80303, USA
[6]Oncology Research & Development, Pfizer Worldwide Research & Development, San Diego, CA 92121, USA
[7]Present address: Transition Bio, Watertown, MA 02472, USA
[8]Present address: LUMICKS, Waltham, MA 02453, USA
[9]Present address: Department of Biochemistry and Molecular Biology, Faculty of Pharmacy, Complutense University of Madrid, 29040 Madrid, Spain
[10]Present address: Josh.ai, Denver, CO 80202, USA
[11]Present address: Belharra Therapeutics, San Diego, CA 92121, USA
[12]Present address: Genesis Therapeutics, San Francisco, CA 94080, USA
[13]Present address: Architect Therapeutics, San Diego, CA 92128, USA
[14]These authors contributed equally
[15]Lead contact
*Correspondence: sabrina.spencer@colorado.edu
https://doi.org/10.1016/j.cell.2023.05.013

SUMMARY

CDK2 is a core cell-cycle kinase that phosphorylates many substrates to drive progression through the cell cycle. CDK2 is hyperactivated in multiple cancers and is therefore an attractive therapeutic target. Here, we use several CDK2 inhibitors in clinical development to interrogate CDK2 substrate phosphorylation, cell-cycle progression, and drug adaptation in preclinical models. Whereas CDK1 is known to compensate for loss of CDK2 in *Cdk2*$^{-/-}$ mice, this is not true of acute inhibition of CDK2. Upon CDK2 inhibition, cells exhibit a rapid loss of substrate phosphorylation that rebounds within several hours. CDK4/6 activity backstops inhibition of CDK2 and sustains the proliferative program by maintaining Rb1 hyperphosphorylation, active E2F transcription, and cyclin A2 expression, enabling re-activation of CDK2 in the presence of drug. Our results augment our understanding of CDK plasticity and indicate that co-inhibition of CDK2 and CDK4/6 may be required to suppress adaptation to CDK2 inhibitors currently under clinical assessment.

INTRODUCTION

Cyclin-dependent kinases (CDKs, including CDK4, CDK6, CDK2, and CDK1) comprise the core machinery that drives cells through the cell cycle. The classic model of cell-cycle progression holds that mitogens stimulate the mitogen-activated protein kinase (MAPK) pathway, leading to the expression of D-type cyclins[1–3] and the activation of CDK4/6. In turn, CDK4/6-cyclin D complexes phosphorylate and inactivate the retinoblastoma protein (Rb1),[4–9] liberating E2F to promote transcription of cyclins E and A, which activate CDK2. Activated CDK2 hyperphosphorylates Rb1,[5,10] establishing a potent positive feedback loop that ensures the continued expression of cyclins E and A, as well as other proteins that are essential for S phase. Engagement of this positive feedback loop creates sustained Rb hyperphosphorylation and constitutes passage through the restriction point, committing cells to complete the cell cycle.[11–13] As cells complete S phase, cyclin A and then cyclin B form complexes with CDK1 to drive cells through mitosis (Figure 1A).

Of these CDK-cyclin complexes, only CDK1 is universally essential.[14–17] While CDK4/6 plays a key role in inactivating Rb1 to facilitate passage through the restriction point, CDK4 is only essential for pancreatic lineages and reproductive functions,[18] whereas both CDK4 and CDK6 are required for hematopoietic lineages.[15,16] Although CDK2 has a key role in the restriction point and in the initiation of S phase, it is genetically

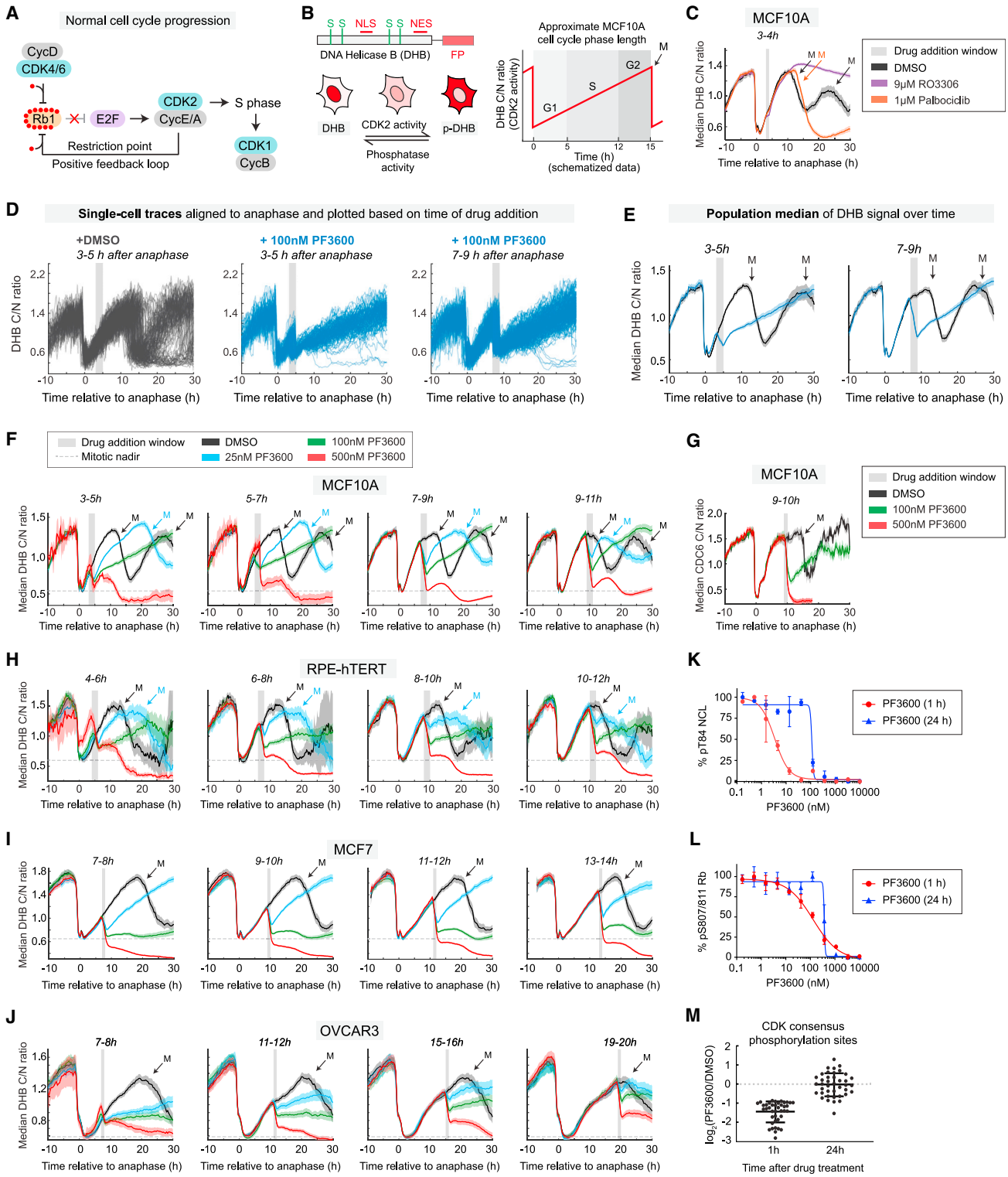

Figure 1. CDK2 activity is acutely inhibited by low-dose PF3600, but phosphorylation rebounds rapidly

(A) Schematic of normal cell-cycle progression.

(B) Left: schematic of the CDK2 activity sensor. DHB (DNA-helicase B fragment) localizes to the nucleus when unphosphorylated; progressive phosphorylation leads to translocation of the sensor to the cytoplasm. NLS, nuclear localization signal; NES, nuclear export signal; S, CDK consensus phosphorylation sites on serine. Right: schematized data showing the dynamics of CDK2 activity across G1, S, G2, and M phases of the cell cycle in MCF10A cells.

(legend continued on next page)

dispensable under normal conditions, as its absence is compensated by CDK1 in *Cdk2*$^{-/-}$ mice.[14,16,19] Nevertheless, CDK2 remains a highly attractive cancer drug target because its aberrant activation, through the formation of non-canonical complexes or by cyclin E amplification,[20–26] can promote hyper-proliferation and confer resistance to FDA-approved CDK4/6 inhibitors.[20,21,27] At least five CDK2 inhibitors have been developed for clinical investigation: PF-06873600 from Pfizer (hereafter PF3600), PF-07104091 from Pfizer (hereafter PF4091), BLU-222 from Blueprint Medicines, INX-315 from Incyclix Bio, and INCB123667 from Incyte.[28–34] In addition, other CDK2 inhibitors and CDK2 degrader modalities are in preclinical development at other companies.

Here, we use single-cell time-lapse imaging of the DNA helicase B (DHB)-based reporter of CDK2 activity[12] (Figure 1B) along with other analyses to assess the acute response to the CDK2 inhibitor PF3600.[33,34] While treatment of cells with PF3600 leads to an immediate reduction of CDK2 kinase activity, these cells rapidly adapt via a CDK2/4/6-Rb-E2F-dependent mechanism that circumvents CDK2 inhibition and enables cell-cycle completion.

RESULTS

Inhibition of CDK2 activity causes loss of substrate phosphorylation followed by a rapid rebound

We first validated the specificity of the DHB-based reporter for CDK2 by treating non-transformed MCF10A cells with RO3306 (CDK1 inhibitor) and Palbociclib (CDK4/6 inhibitor). Neither drug caused a drop in the DHB reporter signal at the time of treatment, consistent with use of this reporter as a readout for CDK2 activity (Figure 1C). As expected, RO3306 induced a G2/M arrest,[12,35] whereas Palbociclib, administered at mid-G1 or later, had no effect on the DHB signal in the ongoing cell cycle. Instead, Palbociclib caused cells to enter a CDK2-low quiescence after the subsequent mitosis, as seen previously,[4,12,36] consistent with the widely held notion that CDK4/6 activity is only required in early G1[37,38] (Figures 1C and S1A).

We next examined the effect of treating cells with a CDK2 inhibitor. PF3600 at low doses (25–100 nM) primarily targets CDK2 and at a high dose (500 nM) blocks the activity of CDK2 and CDK4/6 complexes.[33,34] When we treated MCF10A cells with low-dose PF3600, we observed an immediate and expected drop in CDK2 substrate (DHB) phosphorylation. Surprisingly, however, this was followed by a rapid rebound in activity beginning 1–2 h after drug treatment (hereafter "drop-rebound") (Figures 1D–1F and Videos S1 and S2). Cells eventually completed the cell cycle and mitosis, albeit at a slower rate than DMSO-treated cells (Figures S1B and S1C and Video S1). A rebound in enzyme activity a few hours after its chemical inhibition is highly unusual and would be difficult to detect without a live-cell enzyme activity sensor and high temporal resolution microscopy.

In contrast to the low-dose PF3600 treatments, cells treated with a high dose of PF3600 that covers CDK2, 4, and 6 exhibited a drop followed by a short-lived rebound of about 5 h followed by a sustained crash in CDK2 substrate (DHB) phosphorylation (hereafter referred to as "hump-crash") (Figure 1F). We noted that inhibition of CDK2 to levels where the DHB reporter falls below the mitotic nadir (the lowest CDK2 activity observed in untreated cells) appears to be required for sustained cell-cycle exit. These responses were mirrored with an orthogonal live-cell readout of CDK2 activity, YFP-tagged CDC6[39,40] (Figure 1G). Importantly, the drop-rebound phenotype seen at low doses of PF3600 was not a result of drug degradation, sequestration, or efflux, as refreshing the drug after 5, 10, or 20 h did not alter the response (Figure S1D).

We observed similar responses to the inhibition of CDK2 in the non-transformed cell line RPE-hTERT and the breast adenocarcinoma cell line MCF7, although MCF7 cells displayed greater sensitivity to low-dose PF3600 (Figures 1H, 1I, and S1E–S1G and Videos S3 and S4). The cyclin E-overexpressing ovarian cancer line, OVCAR3, was more responsive to low-dose PF3600, consistent with its known dependence on CDK2,[41] albeit with heterogeneity in the single-cell drug response trajectories (Figures 1J and S1H and Video S5).

We next investigated whether the drop-rebound phenomenon was specific to the DHB- and CDC6-based reporters or whether it occurred broadly across other CDK2 substrates. We first tested the effects of low-dose PF3600 treatment on the CDK2

(C) DHB sensor phosphorylation in MCF10A cells treated with Palbociclib or RO3306. Unless stated otherwise, all plots with DHB cytoplasmic/nuclear (C/N) ratio on the y axis are median ± 95% confidence interval as shaded bands where non-overlapping shading indicates a statistically significant difference with a p value < 0.05 (see Figure S1A). Actively proliferating cells (CDK2^{inc}, see STAR Methods) are selected for plotting if they received drug *t* h after anaphase (gray bar). After the drug addition window, drugs were maintained in the media for the duration of the experiment. M, timing of mitosis, with color matched to legend. Sample size statistics for all experiments are in Table S1.

(D) Single-cell traces of DHB sensor phosphorylation in MCF10A cells treated with DMSO or PF3600. Traces are computationally aligned to the point of anaphase and selected for plotting if they received drug *t* h after anaphase (gray bar). Two time slices are plotted, showing the effect of drug addition at two different points in the cell cycle.

(E) Median DHB sensor phosphorylation over time from the single-cell traces shown in (D), ± 95% confidence interval as shaded bands, as described in (C).

(F) DHB sensor phosphorylation in MCF10A as in (E). Cells were selected for plotting if they completed anaphase *t* h before drug addition, where *t* was selected to sample the cell cycle between 25% and 75% of the intermitotic time. Dotted line marks mitotic nadir.

(G) CDC6 phosphorylation in MCF10A cells as read out by CDC6-YFP C/N ratio. Note that prolonged loss of phosphorylation with 500 nM PF3600 results in degradation of CDC6 by the APC, after which it is not possible to calculate the C/N ratio.

(H–J) DHB sensor phosphorylation as in (E) shown for RPE-hTERT (H), MCF7 (I), and OVCAR3 (J) cells.

(K and L) MCF10A cells were treated with increasing doses of PF3600 for 1 h or 24 h, and phospho-NCL (T84) (K) or phospho-Rb (S807/811) (L) was measured by ELISA. Mean of 2 technical replicates plotted ± SD.

(M) MCF7 cells were treated with 25 nM PF3600, and phosphorylated peptides were assessed by proteomics. Shown are significantly modulated phosphorylated peptides containing a minimal CDK consensus motif (SP or TP) after 1 h treatment ($p < 0.05$) and the fate of those same peptides at 24 h. Data are plotted relative to DMSO control (see Table S2 for raw data).

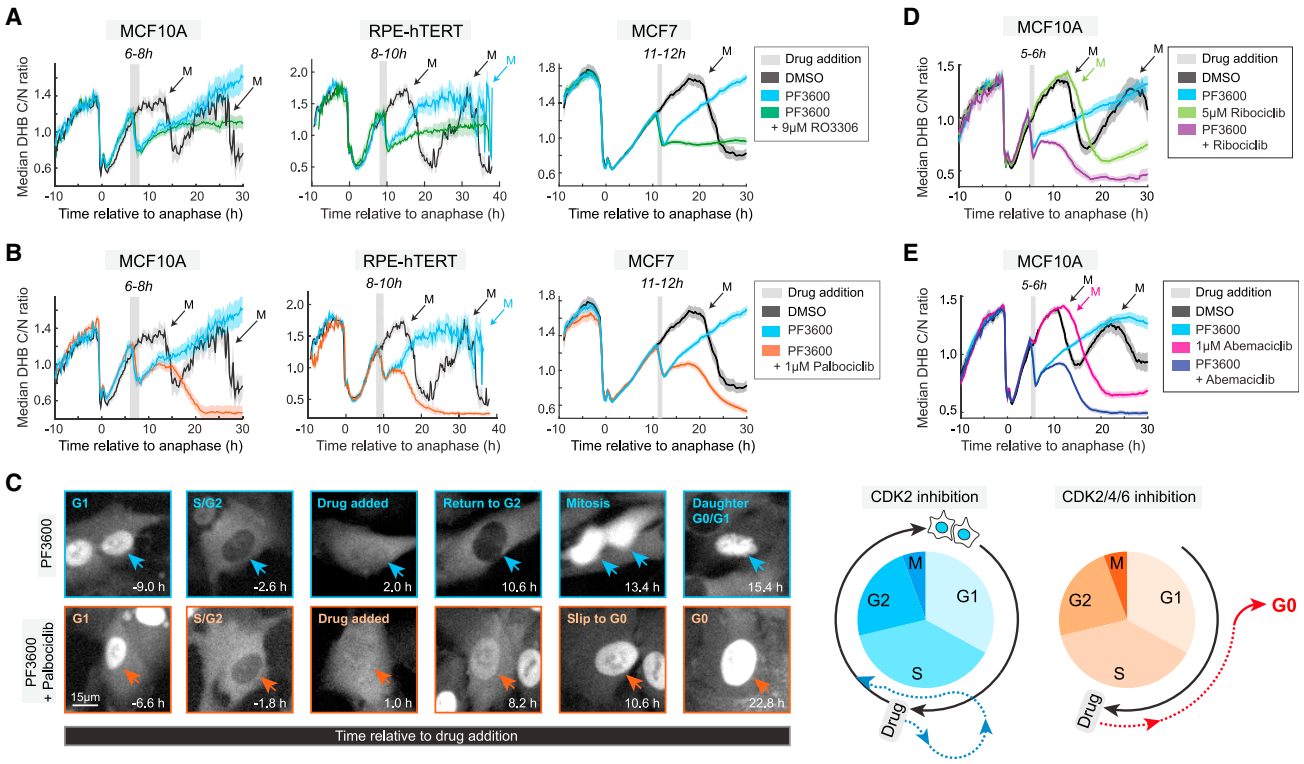

Figure 2. Co-inhibition of CDK2 and CDK4/6 blocks the rebound in CDK2 activity

(A and B) DHB sensor phosphorylation in the three indicated cell lines treated with PF3600 in combination with RO3306 (A) or Palbociclib (B). For MCF10A and RPE-hTERT, 100 nM PF3600 was used; for MCF7, 25 nM PF3600 was used. See also Figure S2 for additional windows of drug addition.

(C) Representative images of the CDK2 sensor over time in RPE-hTERT cells treated with 100 nM PF3600 alone or in combination with Palbociclib. Corresponding schematics of cell-cycle effects are shown to the right.

(D and E) DHB sensor phosphorylation in MCF10A cells treated with 100 nM PF3600 in combination with CDK4/6 inhibitors, Ribociclib (D) or Abemaciclib (E).

substrates nucleolin (NCL)[42,43] and Rb1.[44] These substrates exhibited decreased sensitivity to low-dose PF3600 at 24 h relative to 1 h (Figures 1K and 1L), suggesting that cells had adapted to CDK2 inhibition at the later time point. Unbiased phosphoproteomics further revealed that phosphorylation of peptides with a minimal CDK consensus sequence were diminished at 1 h following low-dose PF3600 but recovered by 24 h (Figures 1M and S1I and Table S2). Thus, although inhibition of CDK2 with low-dose PF3600 leads to an immediate drop in phosphorylation of CDK2 substrates, cells adapt rapidly to restore CDK2 substrate phosphorylation and eventually complete the cell cycle. We considered and went on to test three hypotheses to explain this rebound in CDK2 substrate phosphorylation upon CDK2 inhibition: (1) that CDK2 is not being fully inhibited at CDK2-selective doses of PF3600; (2) that the positive feedback loop, in which CDK2 reinforces Rb hyperphosphorylation, liberation of E2F, and transcription of the cyclins that drive CDK2 activity, is so robust that it is difficult to break; and (3) that other kinases are backstopping CDK2 activity in its absence.

CDK4/6 activity stimulates the rebound upon acute CDK2 inhibition

To explore the mechanism underlying the rebound in CDK2 substrate phosphorylation, we treated cells with low-dose PF3600 together with other CDK inhibitors. Since previous studies reported that CDK1 is sufficient to drive the mammalian cell cycle upon genetic deletion of CDK2,[15,16] we hypothesized that the rebound might be driven by CDK1. To mimic the long timescales used in these genetic experiments, we first grew cells in low-dose PF3600 for 1 month to generate a drug-resistant population and then probed CDK2 substrate phosphorylation upon CDK1 inhibition by using RO3306. We observed that PF3600-resistant cells were more sensitive than drug-naïve cells to CDK1 inhibition (Figures S2A and S2B), suggesting that this long period of adaptation to loss of CDK2 activity causes cells to become more dependent on CDK1. This mirrors the situation in long-adapted *Cdk2*$^{-/-}$ mice where CDK1 mitigates loss of CDK2.

We next assessed the acute treatment timescale. Combination treatment of low-dose PF3600 with RO3306 somewhat reduced but did not eliminate the remaining DHB reporter signal and did not block the re-phosphorylation of NCL (Figures 2A and S2C–S2E), indicating that the rebound in CDK2 substrate phosphorylation is not mediated by CDK1 on short timescales. Thus, while CDK1 may partially contribute to the re-phosphorylation of CDK2 substrates, it is not the primary compensatory factor enabling the immediate rebound observed upon treatment with low-dose PF3600.

While low doses of PF3600 that primarily inhibit CDK2 cause the observed drop-rebound phenotype, a high dose of PF3600 that inhibits both CDK2 and CDK4/6 causes the hump-crash phenotype with sustained suppression of CDK2 substrate phosphorylation (Figure 1F). We therefore speculated that CDK4/6 activity might be involved in enabling the rebound. This hypothesis aligns with early work from Tetsu and McCormick,[45] reporting that CDK4 is required for cell-cycle progression in the absence of CDK2. Indeed, combining low-dose PF3600 with Palbociclib recapitulated the hump-crash phenotype seen with 500 nM PF3600, blocked the re-phosphorylation of NCL, and reduced overall cell proliferation with minimal apoptosis (Figures 2B, 2C, and S2F–S2I and Videos S1, S2, S3, and S4). These data support the notion that low-dose PF3600 can be used to inhibit CDK2 activity without significantly perturbing CDK4/6 activity, since only high-dose PF3600 recapitulates the response produced by low-dose PF3600 plus Palbociclib. Importantly, two other FDA-approved CDK4/6 inhibitors, Ribociclib and Abemaciclib, also elicited the same hump-crash phenotype when combined with low-dose PF3600 (Figures 2D and 2E). Furthermore, knockdown of D-type cyclins or CDK4/6 in conjunction with low-dose PF3600 treatment also phenocopied co-inhibition of CDK4/6 and CDK2 (Figures 3A–3D and S3A–S3F). These results are corroborated by immunoblot analysis of phospho-CDC6 and phospho-NCL (Figure 3E), which show that low-dose PF3600 leads to a rebound in substrate phosphorylation but co-treatment with Palbociclib leads to sustained suppression.

We next probed the temporal contributions of CDK1 and CDK4/6 in supporting the rebound. When cells are treated with the CDK1 inhibitor RO3306 at 0, 5, or 10 h after low-dose PF3600, the rebound is sustained (Figure 3F), consistent with a minor contribution of CDK1 in reinforcing CDK2 substrate phosphorylation at short timescales. When the CDK4/6 inhibitor Palbociclib is added simultaneously with low-dose PF3600, the hump-crash phenotype is observed, confirming its contribution to the rapid rebound phenotype. However, if treatment with Palbociclib is delayed by 5 or 10 h after low-dose PF3600, the rebound is sustained and cells undergo mitosis (Figure 3G). Additionally, triple-drugging cells with CDK2, CDK4/6, and CDK1 inhibitors only marginally reduces the activity hump, consistent with minor contributions of CDK1 in the immediate rebound (ranging from 1.8% early in the cell cycle to 26.6% late in the cell cycle; Figures 3H–3J and S3G–S3I). Together, these data highlight an immediate requirement for CDK4/6 in enabling the rebound upon acute CDK2 inhibition.

CDK4/6 backstops CDK2 to maintain Rb1 hyperphosphorylation throughout S phase

CDK4/6 activity is thought to be critical only for passage through the restriction point in G1.[4,38] Consistently, CDK4/6 inhibition blocks Rb1 phosphorylation in cells with 2N DNA content but does not affect the phosphorylation status of Rb1 in S and G2 phases (Figures 4A [column 2], 4C, and S4A–S4C), as shown previously.[4] This is widely believed to result from the fact that CDK2 takes over hyperphosphorylation of Rb1 once cells have crossed the restriction point.[5,46] Unexpectedly, single-cell immunofluorescence revealed that CDK2 inhibition with low-dose PF3600 barely affected Rb1 phosphorylation in S and G2 phases (Figures 4A [column 3–4], 4C, and S4A–S4E) despite being effective at reducing phosphorylation of NCL, our positive control (Figures 4B [column 3–4], 4C, and S4A–S4C). Instead, either high-dose PF3600 or the combination of low-dose PF3600 plus Palbociclib was required to reduce phosphorylation of Rb1 in S phase (Figures 4A [column 5–6], 4C, and S4A–S4C). Similarly, use of an alternative CDK2 inhibitor, CVT-313, does not affect Rb1 phosphorylation but strongly inhibits phosphorylation of NCL (Figures 4A [column 7], 4C, and S4A–S4C). Neither inhibiting CDK1 nor co-inhibiting CDK2 plus CDK1 results in loss of Rb phosphorylation, and triple-drugging cells for CDK1/2/4/6 offers little additional effect on loss of Rb phosphorylation relative to CDK2/4/6 inhibition (Figures S4F and S4G), consistent with a minor role for CDK1 in the rebound.

The minimal effect on Rb1 phosphorylation upon CDK2 inhibition calls into question the accepted model that CDK2 is solely responsible for hyperphosphorylation of Rb1 in S phase. Our results suggest that enough CDK4/6 activity persists throughout S phase to insulate cells from abrupt shocks to CDK2 activity, a phenomenon only revealed via acute inhibition of CDK2. This resilience of Rb1 phosphorylation in the face of acute reduction of CDK2 activity suggests that the pro-proliferative transcriptional program regulated by the Rb-E2F axis remains active and may drive the observed rebound in CDK2 substrate phosphorylation.

Rb1 status determines rebound capability

To test whether the rebound in CDK2 substrate phosphorylation following CDK2 inhibition is dependent upon Rb1, we utilized CRISPR or siRNA to knock out or knock down Rb1 in MCF10A cells (Figure S4H) and examined the response to CDK inhibition. Apart from making cells cycle slightly faster, knockout or knockdown of Rb1 had minimal effect on cells treated with DMSO (Figures 4D and S4I). The knockout/knockdown conferred resistance to Palbociclib as expected,[20,47,48] visualized as an increase in cell-cycle re-entry after the first mitosis in drug, but had no effect on the response to low-dose PF3600 (Figures 4E, 4F, S4J, and S4K). However, co-inhibition of CDK2 and CDK4/6 with low-dose PF3600 plus Palbociclib elicited a drastically different response in the presence vs. absence of Rb1. Whereas wild-type cells displayed sustained suppression of the DHB reporter signal as in Figure 2B, cells lacking Rb1 showed a rebound in DHB reporter signal even under CDK2 and CDK4/6 co-inhibition (Figures 4G and S4L), phenocopying cells subjected to low-dose PF3600 alone. These data support a model in which CDK4/6 and CDK2 cooperate to maintain Rb1 hyperphosphorylation and E2F liberation to ensure that the cell cycle is completed even in the face of drops in CDK2 or CDK4/6 activity.

We next investigated the expression of E2F1 and cyclins E and A, genes expected to be influenced by the status of Rb1 phosphorylation. Low-dose PF3600 treatment caused upregulation of E2F1 mRNA and protein in wild-type and Rb1-depleted cells. Co-treatment with low-dose PF3600 and Palbociclib strongly blocked E2F1 mRNA and protein upregulation in wild-type cells but not in Rb1-depleted cells at 12 h (Figures 5A, 5B, and S5A). This result was recapitulated for cyclin E1, cyclin E2, and cyclin A2 mRNA and protein (Figures 5A, 5B, S5B, and S5C). The changes in mRNA and protein expression were most

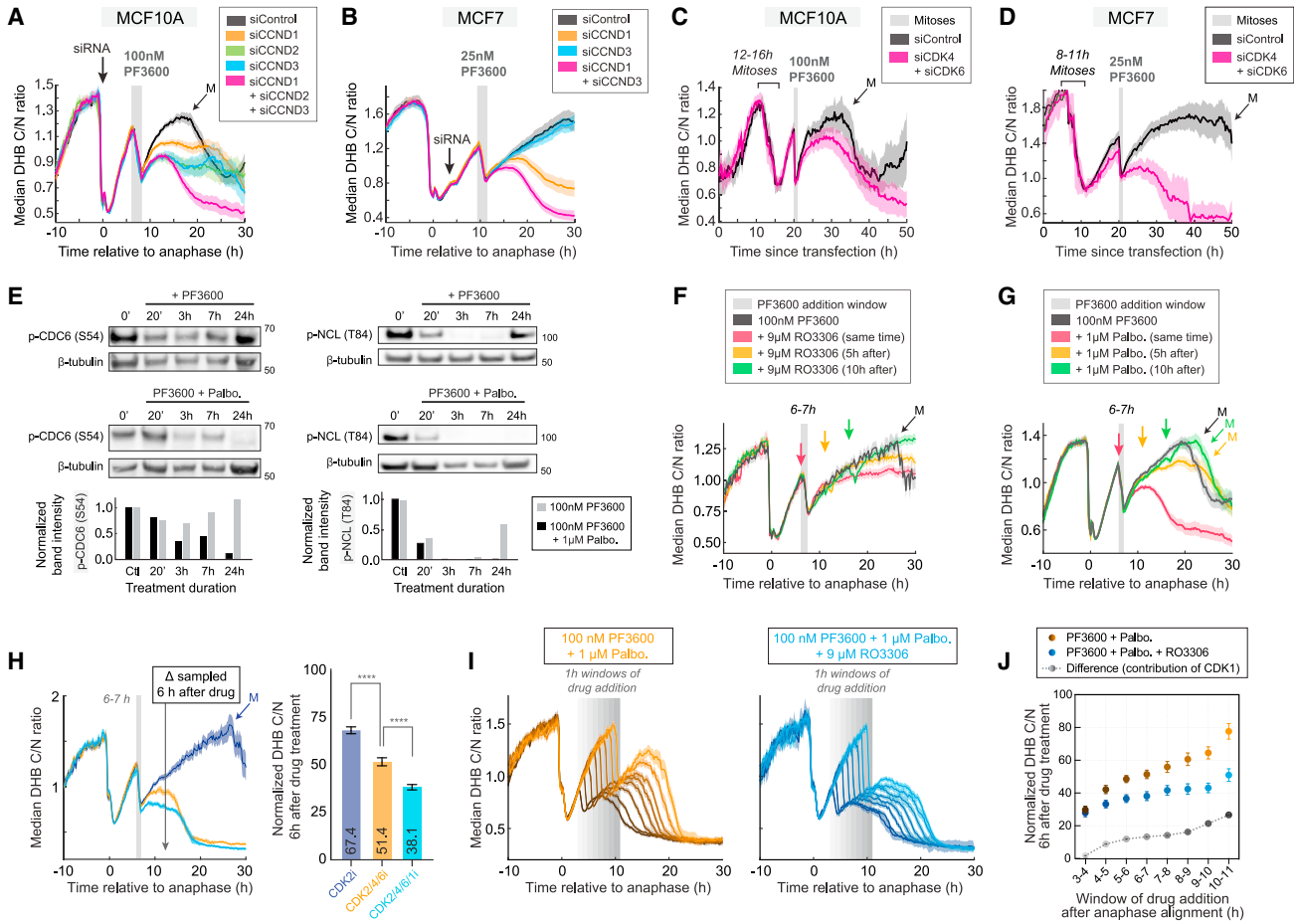

Figure 3. CDK4/6-cyclin D drives the rapid rebound upon CDK2 inhibition

(A and B) DHB sensor phosphorylation in MCF10A (A) and MCF7 (B) treated with low-dose PF3600 (gray bar) 6 h after transfection with the indicated siRNAs (black arrow).

(C and D) DHB sensor phosphorylation in MCF10A (C) and MCF7 (D) treated with low-dose PF3600 20 h after transfection with the indicated siRNAs. x axis represents time since transfection. Cells are plotted if they underwent mitosis *t* h after the time of transfection, where *t* is indicated on the plot by the bracket. Cells are further selected for plotting if they received drug in the window marked by the gray bar.

(E) Western blots showing phosphorylation levels of CDK2 substrates in MCF10A cells after treatment with low-dose PF3600 alone or in combination with Palbociclib for the indicated times. β-tubulin serves as a loading control. Band intensity was quantified and plotted as a bar graph.

(F and G) DHB sensor phosphorylation in MCF10A treated with low-dose PF3600 alone or in combination with RO3306 (F) or Palbociclib (G). Arrows indicate when RO3306 or Palbociclib was added: at the same time as PF3600, 5 h after PF3600, or 10 h after PF3600.

(H) Left: DHB sensor phosphorylation in MCF10A cells after the indicated treatment combinations (doses as in F and G). 6 h after drug addition (gray bar), the DHB C/N ratio was sampled to assess hump magnitude (arrow). Right: Bar plot of normalized DHB signal, where 100% represents the maximum DHB signal reached in an unperturbed cell cycle and 0% represents the floor of the DHB signal (achieved in the triple drug setting). Bars show median value of all cells ± 95% CI.

(I) Overlaid cascade of eight different 1 h drug treatment windows for the indicated conditions.

(J) The median DHB signal was sampled 6 h after each drug treatment and normalized as described in (H). Line plot displays dynamics of the normalized signal across all treatment windows analyzed. Also displayed is the absolute difference between the double and triple drug conditions for each drug window, revealing the relative contribution of CDK1 to the activity hump over the course of the cell cycle. Graph shows median value of all cells ± 95% CI.

See also Figure S3.

pronounced in S-G2 cells, quantified by the percentage of cells with elevated levels (Figures 5A–5C and S5D). In summary, low-dose PF3600 treatment alone increases expression of these key cell-cycle factors, co-treatment with low-dose PF3600 plus Palbociclib reduces their levels, and loss of Rb1 restores their expression to varying degrees. These data support a model in which CDK4/6 maintains Rb1 phosphorylation and E2F activity upon CDK2 inhibition, reinforcing cyclin expression to support a rebound in CDK2 substrate phosphorylation and cell-cycle progression.

Cyclin A2 mediates adaptation to CDK2 inhibition through the Rb-E2F axis

To test the hypothesis that E2F activity supports the rebound in CDK2 substrate phosphorylation, we treated MCF10A cells with the pan-E2F inhibitor HLM006474[49] and examined the response

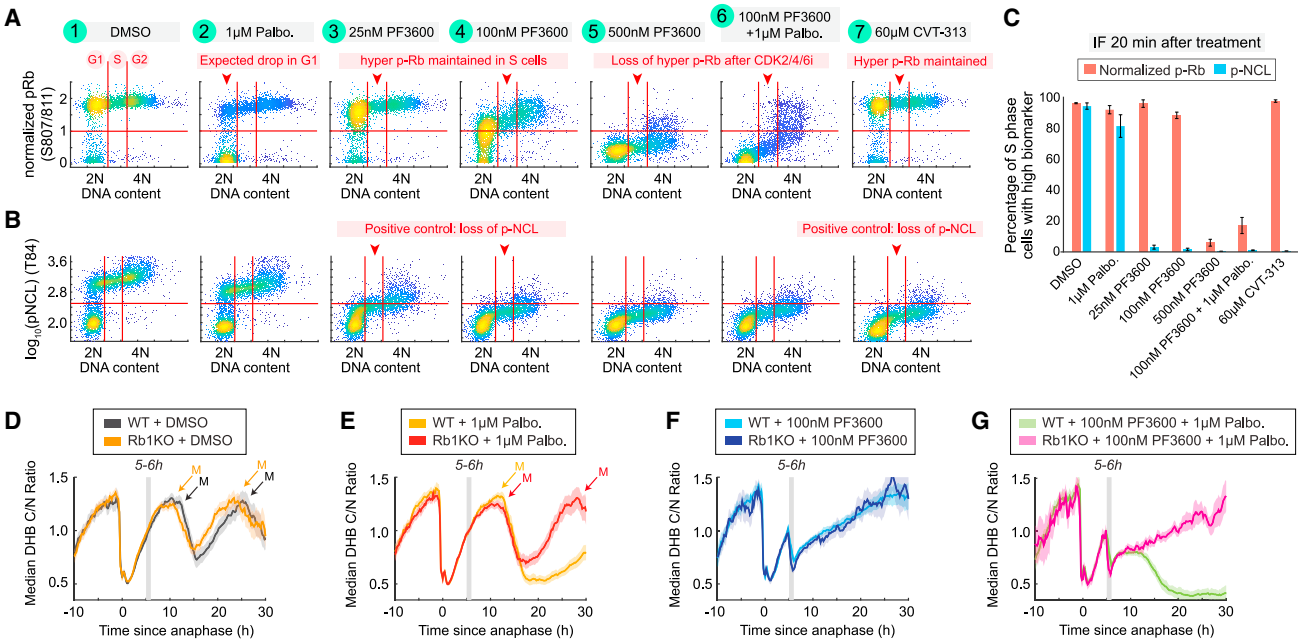

Figure 4. The CDK2 rebound upon low-dose PF3600 treatment depends on Rb1 status

(A and B) Density scatterplots portraying the effect of the indicated compound on pRb (A) and pNCL (B) in MCF10A after 20 min of drug treatment. Red vertical lines indicate gating based on Hoechst stain for subsequent quantification of the S phase population; red horizontal line is set at the midpoint between the high and low populations of normalized phospho-Rb (S807/811) or phospho-NCL (T84) in 2N cells. phospho-Rb was normalized to total Rb in each cell. Note that the top mode of phospho-Rb represents hyperphosphorylated Rb, as shown previously.[4]

(C) Percent of S phase cells from (A) and (B) with high levels of the indicated biomarker after 20 min of drug treatment. Mean of 4 technical replicates plotted ± SD.

(D–G) DHB sensor phosphorylation in WT vs. Rb1 knockout (KO) MCF10A treated with DMSO (D), Palbociclib (E), PF3600 (F), or PF3600 plus Palbociclib (G) at the time marked by the gray bar.

See also Figure S4.

to CDK2 and CDK2/4/6 inhibition. Cells treated with low-dose PF3600 plus E2F inhibitor recapitulated the hump-crash phenotype seen in cells treated with low-dose PF3600 plus Palbociclib (Figures 6A and S6A–S6C), suggesting that E2F activity is required for the rebound.

Hypothesizing that E2F-dependent cyclin production amid CDK2 inhibition may be affecting CDK-cyclin complex profiles, we performed immunoprecipitation experiments after 4 and 12 h of low-dose PF3600. We found that the interaction between CDK2 and cyclin E1 and CDK2 and cyclin A2 increases over time in the presence of low-dose PF3600 (Figures 6B and 6C). Consistent with increased complex formation, treatment with low-dose PF3600 alone led to sustained cyclin E and cyclin A2 mRNA and protein levels, but co-treating with low-dose PF3600 plus Palbociclib or E2F inhibitor caused a strong reduction in cyclin E and cyclin A2 mRNA and protein (Figures 6D, 6E, and S6D).

We next knocked down cyclin E1, cyclin E2, or cyclin A2 (Figure S6E) to assess the extent of each cyclin's contribution to the rebound. In DMSO-treated cells, cyclin E1 is needed to initiate the subsequent cell cycle, whereas cyclin A2 is essential for S phase progression and the continued rise in DHB reporter signal, consistent with prior data (Figure 6F, left).[12] Strikingly, depletion of cyclin A2 (but not cyclin E1 or cyclin E2) compromises the immediate rebound in DHB reporter signal upon low-dose PF3600 treatment (Figure 6F right), suggesting a key role for cyclin A2 in the rebound. We further confirmed the primacy of cyclin A2 in driving the rebound in CDK2 substrate phosphorylation by using an RPE-hTERT line engineered to express cyclin A2 fused to the mAID and SMASh degrons at the endogenous locus.[50] Induced degradation of cyclin A2 combined with low-dose PF3600 eliminates the activity hump and causes immediate and sustained suppression of the DHB reporter signal below the mitotic nadir (Figure 6G).

To visualize the dynamic behavior of cyclin A2 during the rebound, we co-expressed the DHB-based CDK2 reporter in an RPE-hTERT cell line where cyclin A2-mVenus is expressed from the endogenous locus.[51] In unperturbed cells, cyclin A2 begins increasing at the start of S phase and drops in mitosis, as expected (Figure 6H, top left). Upon low-dose PF3600 treatment, cyclin A2 levels continue to rise well beyond the typical cyclin A2 expression maximum (Figure 6H, top middle), whereas co-inhibition of CDK2 and CDK4/6 causes cyclin A2 levels to briefly rise and then crash (Figure 6H, top right). This rise-crash in cyclin A2 levels upon low-dose PF3600 plus Palbociclib mirrors the hump-crash of the DHB reporter signal (Figures 6H, bottom, and S6F–S6H), suggesting that this DHB hump is driven by residual cyclin A2 mRNA that briefly continues to be translated into protein until it decays, resulting in the delayed DHB crash. These observations suggest that continued overproduction of cyclin A2

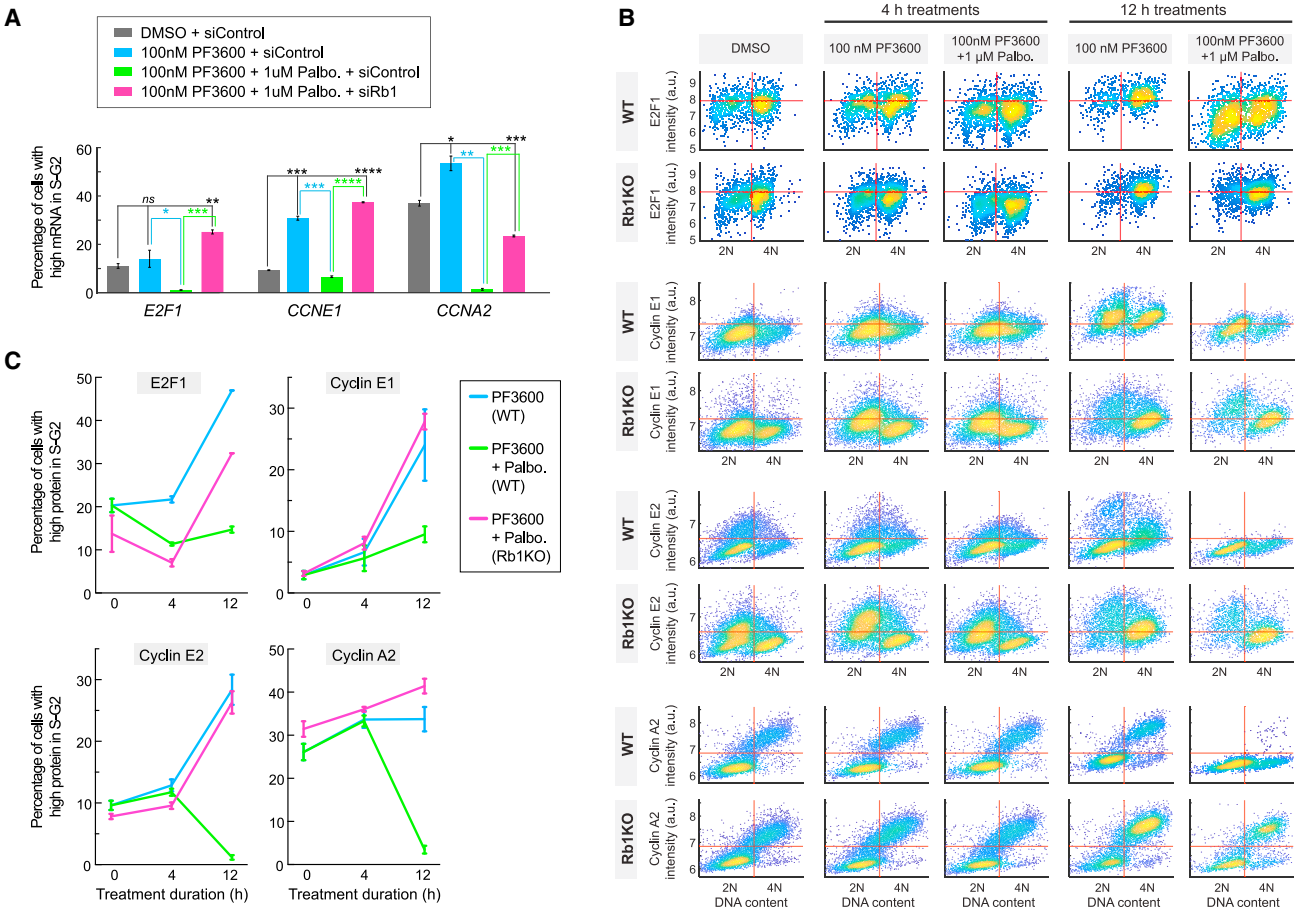

Figure 5. Rb1 status determines cyclin E and A expression in the response to CDK2 inhibition

(A) Quantification of the "S-G2 high" mRNA population for select conditions from Figures S5A–S5C. Each bar indicates the fraction of the total population that can be found in the top-right quadrant. Mean of 2 technical replicates plotted ± SD.

(B) Density scatterplots of E2F1, cyclin E1, cyclin E2, and cyclin A2 nuclear immunofluorescence signal plotted against DNA content in wild-type MCF10A (top) or Rb1KO MCF10A (bottom) treated with the indicated drug for 4 h or 12 h. Red lines indicate gates used to quantify the "S-G2 high" biomarker population in the top-right quadrant.

(C) Quantification of the "S-G2 high" protein population from (B). Each point indicates the fraction of the total population that can be found in the top-right quadrant. Mean of at least 2 technical replicates plotted ± SD.

is a critical adaptive feature of the rebounding cell state. Together, these data delineate a model whereby cyclin A2 production continues to increase amidst CDK2 inhibition, providing a buffer for new CDK2-cyclin A2 complexes to form and outcompete drug pressure.

Cell-cycle progression amidst CDK2 inhibition is sustained by the totality of CDK2/4/6 activities

To determine the generalizability of this adaptation to CDK2 inhibition, we sought to inhibit CDK2 by using orthogonal approaches. Using a CDK2 analog-sensitive ($CDK2^{F80G/F80G}$) RPE-hTERT cell line[52] that is selectively sensitive to the ATP-competitive analog 3MB-PP1, we observed that 3MB-PP1 treatment elicits a similar but muted drop in DHB reporter signal, followed by a rebound (Figures 7A, S7A, and S7B). The muted nature of this drop can be attributed to the $CDK2^{F80G/F80G}$ mutation reducing the function of the native enzyme,[52] which we found causes increased reliance on CDK1 to drive cell-cycle progression (Figure S7C). Co-treatment with 3MB-PP1 plus Palbociclib elicits the hump-crash phenotype (Figure 7A) seen with low-dose PF3600 plus Palbociclib. We also tested the action of two additional inhibitors in clinical development, the CDK2/9 inhibitor, Fadraciclib,[53] and the CDK2-selective inhibitor, PF-07104091[29,54–58] (hereafter PF4091). We found that both drugs recapitulate the drop-rebound in DHB reporter signal seen with low-dose PF3600 treatment and, in combination with Palbociclib, recapitulate the hump-crash in DHB reporter signal and loss of Rb1 phosphorylation (Figures 7B, 7C, and S7D–S7F). Using the RPE-hTERT line where cyclin A2-mVenus is expressed from the endogenous locus, we further found that cyclin A2 expression continues to increase upon PF4091 treatment but is suppressed upon co-treatment with PF4091 and Palbociclib (Figure 7D), recapitulating the results seen with low-dose PF3600

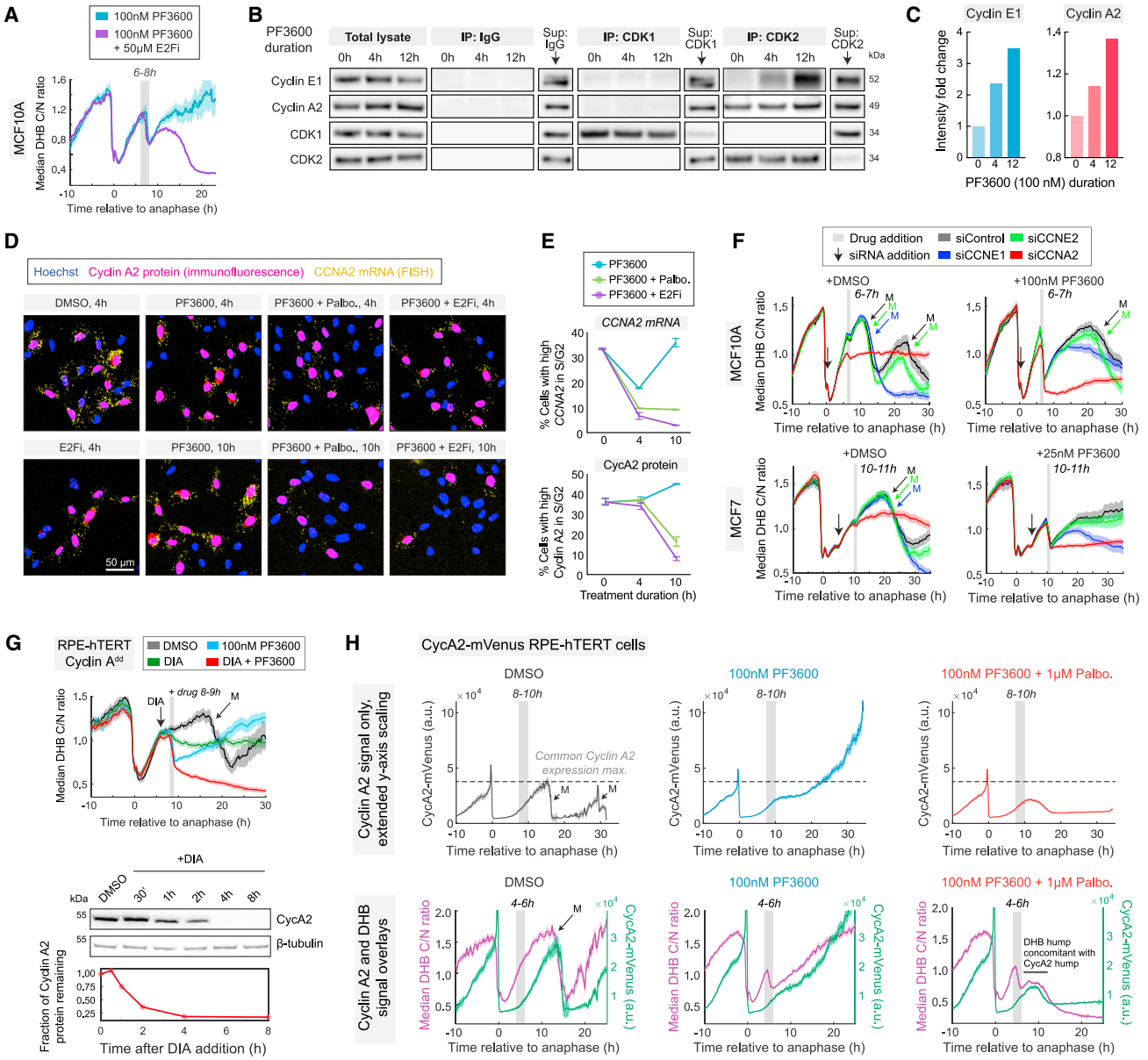

Figure 6. The CDK-Rb1-E2F axis drives cyclin A2 expression to support sustained adaptation to low-dose PF3600

(A) DHB sensor phosphorylation in MCF10A treated with low-dose PF3600, with or without E2Fi.

(B) Immunoprecipitation (IP) and western blot analysis of MCF10A cells treated with 100 nM PF3600 for 0, 4, or 12 h. IgG serves as a negative control. Sup: supernatant, showing that the protein of interest was effectively depleted from the lysate.

(C) Quantification of cyclin E1 and cyclin A2 over time in the CDK2 IP, normalized to the CDK2 band intensity for each time point. Fold change is relative to the 0 h/untreated sample.

(D) Representative images of MCF10A treated with 100 nM PF3600, 1 μM Palbociclib, or 50 μM E2Fi for 4 or 10 h and stained for *CCNA2* mRNA and cyclin A2 protein.

(E) Quantification of the mRNA and protein abundance in S/G2 cells in (D). Mean of 3 technical replicates plotted ± SD.

(F) DHB sensor phosphorylation in MCF10A (top) or MCF7 (bottom) transfected with the indicated siRNAs (black arrow) 6 h before the indicated drug treatments (gray bar).

(G) Top: DHB sensor phosphorylation in RPE-hTERT cells expressing cyclin A2 tagged with a SMASh tag and AID degron from the endogenous *CCNA2* locus. Cells were treated with DMSO or low-dose PF3600 at the time indicated by the gray bar; the doxycycline and indole-3-acetic acid (DIA) treatment used to induce cyclin A2 degradation occurred 2 h before the gray bar, as indicated by the black arrow. Bottom: quantified western blot of cyclin A2 destabilization upon DIA addition, normalized to β-tubulin.

(legend continued on next page)

in Figure 6H. These data show that PF4091 and low-dose PF3600 inhibit CDK2 but leave CDK4/6 and E2F uninhibited to spark the cyclin A2-dependent rebound. By contrast, combination with Palbociclib causes a short-lived "hump" in activity, which is insufficient to maintain E2F-dependent cyclin A2 production.

The observation that none of the CDK2 inhibition strategies tested thus far caused an immediate drop in the DHB reporter signal to below the mitotic nadir led us to suspect that CDK2 was not being fully inhibited in any of these conditions. This would allow the residual CDK2 activity to ignite the rebound, one of our original hypotheses for this phenomenon. To further test this hypothesis, we explored whether CDK2 activity can ever be fully eliminated by drug treatment by applying a supraphysiological dose of PF3600 (10 μM) or PF4091 (20 μM) and observed an immediate crash in DHB reporter signal to below the mitotic nadir with no hump (Figure 7E). While PF3600 may have off-target effects at this dose,[33,34] the complete inhibition of both CDK2 and CDK4/6 permits no rebound whatsoever. The more CDK2-selective PF4091 also resulted in a sustained suppression of DHB reporter signal at the supraphysiological dose, suggesting that potent inhibition of CDK2 alone (without CDK4/6 inhibition) can also inactivate the Rb-E2F axis. These results support the notion that the totality of CDK2, 4, and 6 activities stimulates the immediate rebound and that complete CDK2 inhibition or partial but simultaneous inhibition across CDK2 and CDK4/6 is needed to break the pro-proliferative CDK-Rb-E2F positive feedback loop and push CDK activity below the tipping point, the mitotic nadir.

We next assessed drug responses over a 5-week period. Low-dose PF3600 or Palbociclib only partially suppressed proliferation, whereas low-dose PF3600 plus Palbociclib or high-dose PF3600 caused sustained suppression of growth (Figures 7F, S7G, and S7H and Video S6). A coefficient of drug interaction (CDI) analysis showed that low-dose PF3600 and Palbociclib co-treatment becomes cooperative in suppressing proliferation after a few days (Figure S7I), suggesting that both CDK2 and CDK4/6 must be inhibited to fully block proliferation on an extended timescale.

We tested these predictions by using a mouse lung tumor model driven by $KRAS^{G12V}$ and $TRP53^{L/L}$ mutations. 28 days of Palbociclib treatment did not reduce tumor burden (Figure 7G). An increase in cyclin E expression and CDK2 T-loop phosphorylation[59,60] together with downregulation of p21 (Figure 7H) suggested that this resistance to Palbociclib is driven by an increase in CDK2 activity. Consistently, treatment of these mice with high-dose PF3600 that inhibits both CDK2 and CDK4/6 proved effective at reducing tumor volume while remaining a tolerable therapy (Figures 7H, 7I, S7J, and S7K). To further test this notion, we treated *Cdk2-null* mice from the same $KRAS^{G12V}$;$TRP53^{L/L}$ background with Palbociclib and now observed a significant reduction in tumor volume (Figures 7H, 7I, and S7L). We conclude that ablation of CDK2 renders CDK4/6 inhibition highly effective, but in a wild-type background, CDK2 as well as CDK4/6 must be inhibited to block tumor growth.

DISCUSSION

The concept of CDK plasticity,[61,62] and that CDK1 is largely sufficient for proliferation,[15,16] is well established, but many of these studies relied on genetic methods, which allow for long-term adaptation. Visualization of real-time CDK2 enzyme kinetics in living single cells, together with use of the CDK2 inhibitors PF3600 and PF4091, enabled us to uncover a hard-wired cell-cycle buffering mechanism whereby CDK2 and CDK4/6 backstop one another to keep Rb1 hyperphosphorylated (Figure 7J). This adaptive mechanism does not require cell outgrowth or acquisition of drug-resistance mutations. While acute CDK2 inhibition causes a rapid drop in phosphorylation for most CDK2 substrates, phosphorylation of Rb1 is maintained by CDK4/6 activity. E2F therefore remains active, sustaining cyclin A2 production and a rebound in CDK2 substrate phosphorylation. By contrast, inhibition of both CDK2 and CDK4/6 (but not CDK1) blocks Rb1 phosphorylation and the rebound. These data argue that it is the totality of CDK2/4/6 activity phosphorylating Rb1 that determines whether the cell mounts a rebound or undergoes a sustained crash in CDK2 substrate phosphorylation. Thus, in the contexts examined here, co-inhibition of CDK2 and CDK4/6 is required to undermine a cell's CDK2-increasing proliferative trajectory and break the positive feedback loop that reinforces Rb1 phosphorylation (Figure 7J).

A key question is which CDK activity mediates the rebound in CDK2 substrate phosphorylation. CDK4/6-cyclin D does not typically phosphorylate CDK2 substrates[63] including DHB[12,64] and is unlikely to change its substrate specificity upon CDK2 inhibition. Furthermore, the rebound is strongly cyclin A2 dependent. While CDK1-cyclin A2 may contribute partially to the rebound, Figure 3F suggests that CDK1 is not the dominant kinase mediating the rebound on short timescales. We therefore take the view that the rebound consists primarily of CDK2-cyclin A2 activity. However, this model raises the fundamental question of how CDK2 activity can persist in the presence of a potent CDK2 inhibitor. While the full answer to this question requires additional study, our simplest interpretation of the data, given that knockdown or degradation of cyclin A2 blocks the rebound but knockdown of cyclin E1 or E2 does not (Figures 6F and 6G), is that the CDK2 inhibitors tested here preferentially inhibit CDK2-cyclin E over CDK2-cyclin A, consistent with live-cell NanoBRET measurements.[33] Although PF3600 does inhibit CDK2-cyclin A2 *in vitro*,[33] our study suggests inefficient targeting of CDK2-cyclin A2 complexes inside living cells. Drug-induced stabilization of CDK2-cyclin A2, a phenomenon that has been described recently in other contexts,[65] may contribute to the rebound in CDK2 activity. Taken together, these findings serendipitously emphasize the usefulness of these

(H) Top: cyclin A2-mVenus intensity over time showing the average maximum intensity before mitosis in DMSO-treated cells, how this expression level is surpassed in cells rebounding in low-dose PF3600 treatment, and the rise-crash in cyclin A2 in cells treated with low-dose PF3600 plus Palbociclib. Bottom: Overlay plots of DHB sensor phosphorylation (left axis) and cyclin A2-mVenus intensity (right axis) in RPE-hTERT cells treated with the indicated drugs.
See also Figure S6.

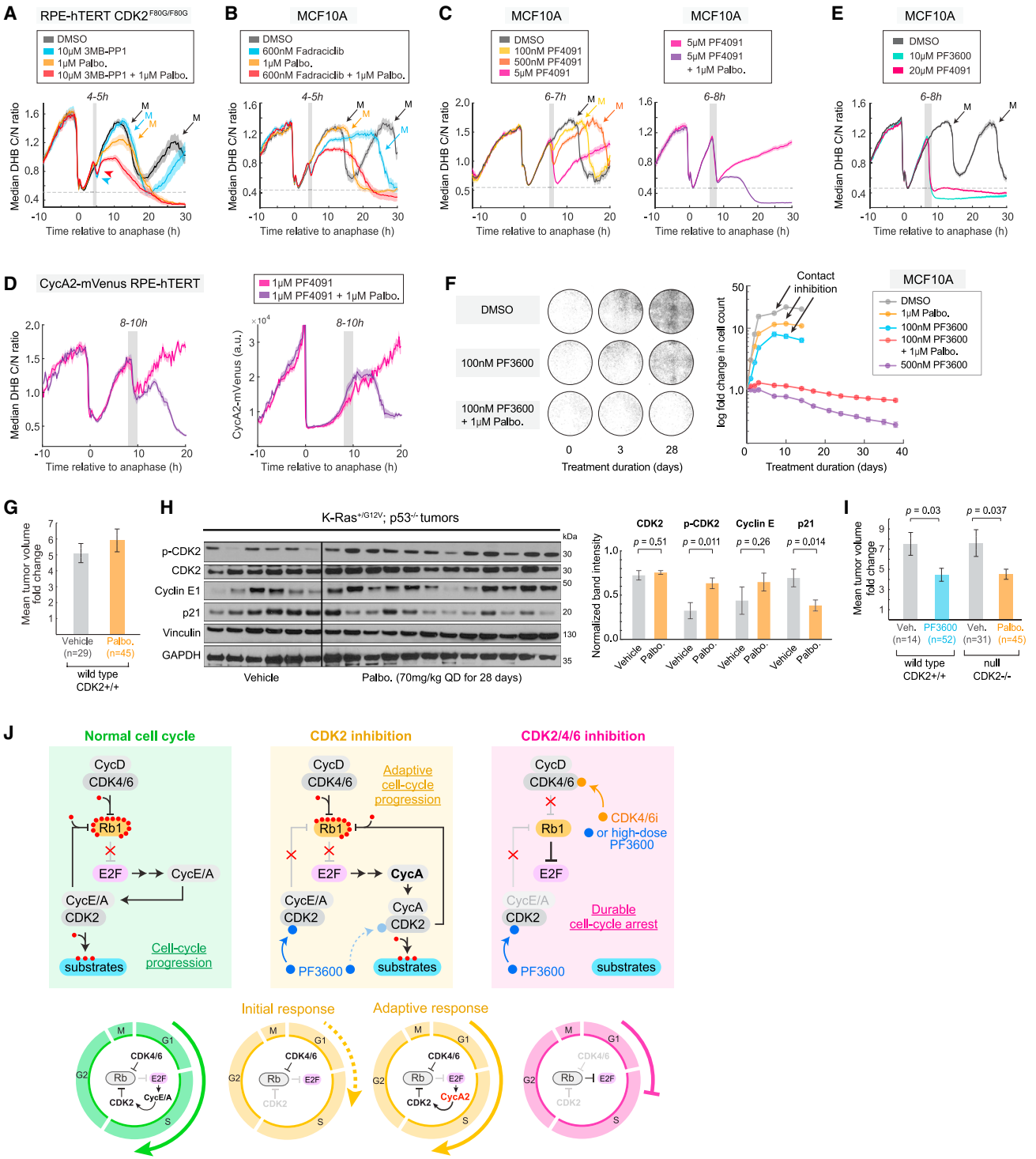

Figure 7. Orthogonal CDK2 inhibition approaches and *in vivo* studies indicate that cell-cycle progression is maintained by the combined sum of CDK2/4/6 activity

(A) DHB sensor phosphorylation in RPE-hTERT CDK2$^{F80G/F80G}$ cells treated with 3MB-PP1 alone or in combination with Palbociclib. Arrowheads mark initial 3MB-PP1-induced drop. Dotted line marks mitotic nadir.

(B and C) DHB sensor phosphorylation in MCF10A cells treated with CDK2 inhibitors Fadraciclib (B) or PF4091 (C), alone or in combination with Palbociclib. Dotted line marks mitotic nadir.

(D) DHB sensor phosphorylation (left) and endogenous cyclin A2-mVenus intensity (right) in RPE-hTERT treated with the indicated drugs at the gray bar.

(legend continued on next page)

CDK2 inhibitors for cancers that are heavily reliant on cyclin E. We therefore conclude that the rebound in CDK2 activity upon acute CDK2 inhibition results from a combination of our original three hypotheses: chemical inhibition of CDK2 activity is incomplete, leaving residual CDK2 activity to maintain the positive feedback loop that sustains cell-cycle commitment, backstopped by CDK4/6's maintenance of Rb hyperphosphorylation.

In 2003, Tetsu and McCormick reported that increased levels of CDK4 in cancer can compensate for loss of CDK2 activity and concluded that CDK2 may not be a suitable target for cancer treatment.[45] However, despite the rebound in CDK2 activity observed on the short timescale studied here, long-term CDK2 inhibition is effective in patient-derived mouse xenografts, particularly for cyclin E-amplified cancers.[33] Cyclin E amplification in tumors can occur as a pre-existing intrinsic oncogenic driver or as an acquired feature of clinical resistance to CDK4/6 inhibitors,[20,21,27] supporting the potential of CDK2 as a therapeutic target.

Our model of latent CDK4/6 activity throughout S phase contrasts with prior classical models, wherein CDK4/6 mono-[5] or hypo-phosphorylates[9,46] Rb1 in G1 to partially liberate E2F,[66] after which CDK2 sustains Rb1 hyperphosphorylation. We are aware of only one prior report showing that CDK4/6 can hyperphosphorylate Rb1 in G1 phase.[4] Our results corroborate this latter view and develop it further by demonstrating maintenance of Rb1 hyperphosphorylation by CDK4/6 beyond G1 and into S phase (Figure 4A). This S phase role of CDK4/6 in the hyperphosphorylation of Rb1 and maintenance of cell-cycle progression has not been previously identified due to a lack of tools to rapidly and specifically inhibit CDK2.

Our results are consistent across several CDK2 inhibitors in clinical development and short-term and long-term cell culture experiments, as well as in mice, where Palbociclib-resistant mouse lung tumors show combinatorial activity of CDK2 ablation and CDK4/6 inhibition similar to inhibition of CDK2/4/6 with high-dose PF3600. While resistance to CDK4/6 inhibition via CDK2 activity has been well established,[20,26,27,67] here we demonstrate the reverse—rapid adaptation to CDK2 inhibition via maintenance of Rb1 hyperphosphorylation by CDK4/6. On extended timescales of CDK2 inhibition, we show a shift from CDK4/6 reliance to CDK1 reliance. Given that CDK1 inhibition is expected to be poorly tolerated in people,[16,68] co-targeting CDK2 and CDK4/6 represents a potential treatment strategy to ablate the early adaptive rebound and stave off more problematic CDK1-mediated adaptation to CDK2 inhibition. Our work suggests that simultaneous combination therapy of CDK2 and CDK4/6 inhibitors may be needed for durable growth inhibition of relevant tumors, an idea that is currently being tested in clinical trials.[28–31] In summary, our study uncovers a hard-wired cell-cycle buffering system, enabling an improved understanding of CDK2/4/6-Rb-E2F plasticity.

Limitations of the study

The rebound in CDK2 substrate phosphorylation appears to be driven by a pool of free or poorly inhibited CDK2 even in the presence of a CDK2 inhibitor, revealing a biological paradox. While we have robustly characterized the cyclin A2 dynamics that foster this rapid drug adaptation, the dynamics of CDK2 complexes and the coupling between cyclin binding and inhibitor binding require further investigation. It is also likely that additional undiscovered CDK regulators could contribute to the rebound phenomenon. Candidates include the CDK inhibitors p16, p18, p21, and p27; the CDK phosphatases CDC25A, B, and C; and the CDK kinases Wee1, Myt1, and CDK7.[69–72] Additionally, while we demonstrate that CDK1's contribution to the rebound is modest on the short timescales examined here, further work is needed to identify how and when CDK1 takes over from CDK4/6 under extended CDK2 inhibition to reach the CDK1-dependent state seen in CDK2-null mice.

STAR★METHODS

Detailed methods are provided in the online version of this paper and include the following:

- KEY RESOURCES TABLE
- RESOURCE AVAILABILITY
  - Lead contact
  - Materials availability
  - Data and code availability
- EXPERIMENTAL MODEL AND SUBJECT DETAILS
  - Cell culture
  - Stable cell line generation using lentiviral vectors
  - RB1 knockout cell line generation
  - Mouse studies
- METHOD DETAILS
  - siRNA transfections
  - Time-lapse imaging
  - Immunofluorescence
  - Apoptosis assay
  - Long-term treatment experiment
  - 7-day treatment experiment

(E) DHB sensor phosphorylation in MCF10A cells treated with supraphysiological doses of PF3600 or PF4091. Dotted line marks mitotic nadir.
(F) Long-term treatment of MCF10A cells with the indicated drugs. Mean of 6 technical replicates plotted ± SD. Representative images from day 0, 3, and 28 for the indicated drug conditions.
(G) Average tumor volume fold change (as measured by CT scans, Figure S7L) from *Kras*$^{+/LSLG12V}$;*Trp53*$^{L/L}$ mice. Measurements were carried out 28 days after Palbociclib treatment (70 mg/kg). n = number of tumors. Mean tumor volume fold change was calculated as final tumor volume divided by initial tumor volume. Error bars indicate SEM.
(H) Western blots of tumors from the Palbociclib treated *Kras*$^{+/LSLG12V}$;*Trp53*$^{L/L}$ mice in (G) probed for the indicated biomarkers and quantified as a bar graph. Error bars indicate SEM from multiple tumors normalized to vinculin for all targets except for p-CDK2, which was normalized to GAPDH. p values are from an unpaired t test.
(I) Mean tumor volume fold change from number of tumors "n" from each cohort of *Kras*$^{+/LSLG12V}$;*Trp53*$^{L/L}$ mice. The CDK2 status is indicated as wild type (CDK2$^{+/+}$) or null (CDK2$^{-/-}$). Tumor volumes are measured by CT scans. Mean tumor volume fold change calculated as in (G). Error bars indicate SEM.
(J) Proposed model of adaptation to CDK2 inhibition.

- Small molecules
- Phospho-serine 807/811 Rb and phospho-threonine 84 NCL ELISA
- Western blotting
- Immunoprecipitation
- mRNA FISH
- Phosphoproteomics

● QUANTIFICATION AND STATISTICAL ANALYSIS
- Cell tracking and single-cell CDK2 activity analysis
- Statistics

SUPPLEMENTAL INFORMATION

Supplemental information can be found online at https://doi.org/10.1016/j.cell.2023.05.013.

ACKNOWLEDGMENTS

We thank members of the Spencer Lab for general help and discussion; Peter Olsen (formerly at Pfizer) for helping establish the collaboration between the Spencer Lab and Pfizer; and Theresa Nahreini for her assistance in cell sorting. The BD FACSCelesta cytometer and BD FACSAria Fusion cell sorter are supported by NIH Grant S10ODO21601. Some imaging work was performed at the BioFrontiers Institute Advanced Light Microscopy Core (RRID: SCR_018302) with the help of Dr. Joseph Dragavon. The PerkinElmer Opera Phenix is supported by NIH grant 1S10OD025072. This work was funded by Pfizer Inc. and by Spencer Lab start-up funding from University of Colorado-Boulder.

AUTHOR CONTRIBUTIONS

M.A. and J.M. conducted the majority of the cell line generation, western blots, live- and fixed-cell imaging experiments; T.E.H. suggested and performed the triple drug experiments, conducted the work regarding cyclin A2 expression dynamics, and performed the majority of the figure preparation for the manuscript; L.P.W. conducted the work regarding alternative CDK2 and CDK4/6 inhibitors and long-term treatments and assisted with many experiments; M. Min suggested and performed Rb siRNA experiments; Y.R. generated the Rb1-knockout cells; C.R.I. and V.N. performed the immunoprecipitation experiments; J.S. conducted live-cell experiments with CDC6-YFP; M. Musteanu conducted the mouse lung and tumor model studies and M.S. performed the associated western blots under the direction of M.B.; S.N. designed and analyzed the mass spectrometry; J.L. conducted the mass spectrometry; L.N. generated samples for the mass spectrometry and conducted ELISA assays; N.M. designed ELISA assays and analyzed data; S.L.S., T.V., and N.M. conceived the original study idea; S.L.S. oversaw the study, suggested the experiments, and interpreted the data together with M.A., J.M., T.E.H., L.P.W., M. Min, N.M., S.D., and T.V. M.A., J.M., T.E.H., L.P.W., and S.L.S. wrote the manuscript with input from S.D. and N.M.

DECLARATION OF INTERESTS

The authors declare the following competing interests: S.L.S. received research funding from Pfizer Inc. for this collaboration. Pfizer authors were involved in the conceptualization and design of the study and performed their own data collection and analysis where indicated. Pfizer authors also provided input on the manuscript. M.B. received research funding from Pfizer Inc. S.D. and T.V. are stockholders of Pfizer Inc. A joint patent related to this work has been filed by the Regents of the University of Colorado and Pfizer Inc, with authors S.L.S., M.A., S.D., N.M., and T.V. Application number: PCT/IB2021/052894. Status of application: pending. Specific aspect of manuscript covered in the patent application involves co-treatment with CDK4/6 and CDK2 inhibitors to suppress adaptation to CDK2 inhibitors.

Received: November 3, 2020
Revised: October 10, 2022
Accepted: May 10, 2023
Published: June 1, 2023

REFERENCES

1. Aktas, H., Cai, H., and Cooper, G.M. (1997). Ras links growth factor signaling to the cell cycle machinery via regulation of cyclin D1 and the Cdk inhibitor p27KIP1. Mol. Cell Biol. *17*, 3850–3857. https://doi.org/10.1128/mcb.17.7.3850.
2. Sherr, C.J. (1994). G1 phase progression: Cycling on cue. Cell *79*, 551–555. https://doi.org/10.1016/0092-8674(94)90540-1.
3. Sherr, C.J. (1993). Mammalian G1 cyclins. Cell *73*, 1059–1065. https://doi.org/10.1016/0092-8674(93)90636-5.
4. Chung, M., Liu, C., Yang, H.W., Köberlin, M.S., Cappell, S.D., and Meyer, T. (2019). Transient Hysteresis in CDK4/6 Activity Underlies Passage of the Restriction Point in G1. Mol. Cell *76*, 562–573.e4. https://doi.org/10.1016/j.molcel.2019.08.020.
5. Narasimha, A.M., Kaulich, M., Shapiro, G.S., Choi, Y.J., Sicinski, P., and Dowdy, S.F. (2014). Cyclin D activates the Rb tumor suppressor by mono-phosphorylation. Elife *3*, e02872. https://doi.org/10.7554/eLife.02872.
6. Sanidas, I., Morris, R., Fella, K.A., Rumde, P.H., Boukhali, M., Tai, E.C., Ting, D.T., Lawrence, M.S., Haas, W., and Dyson, N.J. (2019). A Code of Mono-phosphorylation Modulates the Function of RB. Mol. Cell *73*, 985–1000.e6. https://doi.org/10.1016/j.molcel.2019.01.004.
7. Matsushime, H., Quelle, D.E., Shurtleff, S.A., Shibuya, M., Sherr, C.J., and Kato, J.Y. (1994). D-type cyclin-dependent kinase activity in mammalian cells. Mol. Cell Biol. *14*, 2066–2076. https://doi.org/10.1128/mcb.14.3.2066.
8. Kato, J., Matsushime, H., Hiebert, S.W., Ewen, M.E., and Sherr, C.J. (1993). Direct binding of cyclin D to the retinoblastoma gene product (pRb) and pRb phosphorylation by the cyclin D-dependent kinase CDK4. Genes Dev. *7*, 331–342. https://doi.org/10.1101/gad.7.3.331.
9. Ezhevsky, S.A., Nagahara, H., Vocero-Akbani, A.M., Gius, D.R., Wei, M.C., and Dowdy, S.F. (1997). Hypo-phosphorylation of the retinoblastoma protein (pRb) by cyclin D:Cdk4/6 complexes results in active pRb. Proc. Natl. Acad. Sci. USA *94*, 10699–10704. https://doi.org/10.1073/pnas.94.20.10699.
10. Harbour, J.W., Luo, R.X., Dei Santi, A., Postigo, A.A., and Dean, D.C. (1999). Cdk Phosphorylation Triggers Sequential Intramolecular Interactions that Progressively Block Rb Functions as Cells Move through G1. Cell *98*, 859–869. https://doi.org/10.1016/S0092-8674(00)81519-6.
11. Pardee, A.B. (1974). A Restriction Point for Control of Normal Animal Cell Proliferation. Proc. Natl. Acad. Sci. USA *71*, 1286–1290. https://doi.org/10.1073/pnas.71.4.1286.
12. Spencer, S.L., Cappell, S.D., Tsai, F.-C., Overton, K.W., Wang, C.L., and Meyer, T. (2013). The Proliferation-Quiescence Decision Is Controlled by a Bifurcation in CDK2 Activity at Mitotic Exit. Cell *155*, 369–383. https://doi.org/10.1016/j.cell.2013.08.062.
13. Weinberg, R.A. (1995). The retinoblastoma protein and cell cycle control. Cell *81*, 323–330. https://doi.org/10.1016/0092-8674(95)90385-2.
14. Berthet, C., Aleem, E., Coppola, V., Tessarollo, L., and Kaldis, P. (2003). Cdk2 knockout mice are viable. Curr. Biol. *13*, 1775–1785. https://doi.org/10.1016/j.cub.2003.09.024.
15. Malumbres, M., Sotillo, R., Santamaría, D., Galán, J., Cerezo, A., Ortega, S., Dubus, P., and Barbacid, M. (2004). Mammalian Cells Cycle without the D-Type Cyclin-Dependent Kinases Cdk4 and Cdk6. Cell *118*, 493–504. https://doi.org/10.1016/j.cell.2004.08.002.
16. Santamaría, D., Barrière, C., Cerqueira, A., Hunt, S., Tardy, C., Newton, K., Cáceres, J.F., Dubus, P., Malumbres, M., and Barbacid, M. (2007). Cdk1 is sufficient to drive the mammalian cell cycle. Nature *448*, 811–815. https://doi.org/10.1038/nature06046.

17. Knudsen, E.S., Kumarasamy, V., Nambiar, R., Pearson, J.D., Vail, P., Rosenheck, H., Wang, J., Eng, K., Bremner, R., Schramek, D., et al. (2022). CDK/cyclin dependencies define extreme cancer cell-cycle heterogeneity and collateral vulnerabilities. Cell Rep. *38*, 110448. https://doi.org/10.1016/j.celrep.2022.110448.

18. Tsutsui, T., Hesabi, B., Moons, D.S., Pandolfi, P.P., Hansel, K.S., Koff, A., and Kiyokawa, H. (1999). Targeted Disruption of CDK4 Delays Cell Cycle Entry with Enhanced p27 ^{Kip1} Activity. Mol. Cell Biol. *19*, 7011–7019. https://doi.org/10.1128/MCB.19.10.7011.

19. Ortega, S., Prieto, I., Odajima, J., Martín, A., Dubus, P., Sotillo, R., Barbero, J.L., Malumbres, M., and Barbacid, M. (2003). Cyclin-dependent kinase 2 is essential for meiosis but not for mitotic cell division in mice. Nat. Genet. *35*, 25–31. https://doi.org/10.1038/ng1232.

20. Herrera-Abreu, M.T., Palafox, M., Asghar, U., Rivas, M.A., Cutts, R.J., Garcia-Murillas, I., Pearson, A., Guzman, M., Rodriguez, O., Grueso, J., et al. (2016). Early Adaptation and Acquired Resistance to CDK4/6 Inhibition in Estrogen Receptor-Positive Breast Cancer. Cancer Res. *76*, 2301–2313. https://doi.org/10.1158/0008-5472.CAN-15-0728.

21. Franco, J., Witkiewicz, A.K., and Knudsen, E.S. (2014). CDK4/6 inhibitors have potent activity in combination with pathway selective therapeutic agents in models of pancreatic cancer. Oncotarget *5*, 6512–6525. https://doi.org/10.18632/oncotarget.2270.

22. Keyomarsi, K., Tucker, S.L., Buchholz, T.A., Callister, M., Ding, Y., Hortobagyi, G.N., Bedrosian, I., Knickerbocker, C., Toyofuku, W., Lowe, M., et al. (2002). Cyclin E and survival in patients with breast cancer. N. Engl. J. Med. *347*, 1566–1575. https://doi.org/10.1056/NEJMoa021153.

23. Yang, C., Li, Z., Bhatt, T., Dickler, M., Giri, D., Scaltriti, M., Baselga, J., Rosen, N., and Chandarlapaty, S. (2017). Acquired CDK6 amplification promotes breast cancer resistance to CDK4/6 inhibitors and loss of ER signaling and dependence. Oncogene *36*, 2255–2264. https://doi.org/10.1038/onc.2016.379.

24. Marone, M., Scambia, G., Giannitelli, C., Ferrandina, G., Masciullo, V., Bellacosa, A., Benedetti-Panici, P., and Mancuso, S. (1998). Analysis of cyclin E and CDK2 in ovarian cancer: Gene amplification and RNA overexpression. Int. J. Cancer *75*, 34–39. https://doi.org/10.1002/(SICI)1097-0215(19980105)75:1<34::AID-IJC6>3.0.CO;2-2.

25. Harwell, R.M., Mull, B.B., Porter, D.C., and Keyomarsi, K. (2004). Activation of Cyclin-dependent Kinase 2 by Full Length and Low Molecular Weight Forms of Cyclin E in Breast Cancer Cells. J. Biol. Chem. *279*, 12695–12705. https://doi.org/10.1074/jbc.M313407200.

26. Walter, D.M., Yates, T.J., Ruiz-Torres, M., Kim-Kiselak, C., Gudiel, A.A., Deshpande, C., Wang, W.Z., Cicchini, M., Stokes, K.L., Tobias, J.W., et al. (2019). RB constrains lineage fidelity and multiple stages of tumour progression and metastasis. Nature *569*, 423–427. https://doi.org/10.1038/s41586-019-1172-9.

27. Turner, N.C., Liu, Y., Zhu, Z., Loi, S., Colleoni, M., Loibl, S., DeMichele, A., Harbeck, N., André, F., Bayar, M.A., et al. (2019). Cyclin E1 Expression and Palbociclib Efficacy in Previously Treated Hormone Receptor–Positive Metastatic Breast Cancer. J. Clin. Orthod. *37*, 1169–1178. https://doi.org/10.1200/JCO.18.00925.

28. Pfizer (2022). A Study to Learn about the Study Medicine (Called PF-07220060 in Combination with PF-07104091) in Participants with Breast Cancer and Solid Tumors. NCT05262400.

29. Pfizer (2020). PF-07104091 as a Single Agent and in Combination Therapy. NCT04553133.

30. Blueprint Medicines Corporation (2022). (VELA) Study of BLU-222 in Advanced Solid Tumors. NCT05252416.

31. Incyclix Bio (2023). Open-Label Study to Evaluate the Safety, Tolerability, PK, and Efficacy of INX-315 in Patients with Advanced Cancer (INX-315-01). NCT05735080.

32. Incyte Corporation (2022). Study of INCB123667 in Subjects with Advanced Solid Tumors. NCT05238922.

33. Freeman-Cook, K., Hoffman, R.L., Miller, N., Almaden, J., Chionis, J., Zhang, Q., Eisele, K., Liu, C., Zhang, C., Huser, N., et al. (2021). Expanding control of the tumor cell cycle with a CDK2/4/6 inhibitor. Cancer Cell *39*, 1404–1421.e11. https://doi.org/10.1016/j.ccell.2021.08.009.

34. Freeman-Cook, K.D., Hoffman, R.L., Behenna, D.C., Boras, B., Carelli, J., Diehl, W., Ferre, R.A., He, Y.-A., Hui, A., Huang, B., et al. (2021). Discovery of PF-06873600, a CDK2/4/6 Inhibitor for the Treatment of Cancer. J. Med. Chem. *64*, 9056–9077. https://doi.org/10.1021/acs.jmedchem.1c00159.

35. Vassilev, L.T. (2006). Cell Cycle Synchronization at the G2/M Phase Border by Reversible Inhibition of CDK1. Cell Cycle *5*, 2555–2556. https://doi.org/10.4161/cc.5.22.3463.

36. Yang, H.W., Cappell, S.D., Jaimovich, A., Liu, C., Chung, M., Daigh, L.H., Pack, L.R., Fan, Y., Regot, S., Covert, M., and Meyer, T. (2020). Stress-mediated exit to quiescence restricted by increasing persistence in CDK4/6 activation. Elife *9*, e44571. https://doi.org/10.7554/eLife.44571.

37. Min, M., Rong, Y., Tian, C., and Spencer, S.L. (2020). Temporal integration of mitogen history in mother cells controls proliferation of daughter cells. Science *368*, 1261–1265. https://doi.org/10.1126/science.aay8241.

38. Sherr, C.J., and Roberts, J.M. (2004). Living with or without cyclins and cyclin-dependent kinases. Genes Dev. *18*, 2699–2711. https://doi.org/10.1101/gad.1256504.

39. Petersen, B.O., Lukas, J., Sørensen, C.S., Bartek, J., and Helin, K. (1999). Phosphorylation of mammalian CDC6 by cyclin A/CDK2 regulates its subcellular localization. EMBO J. *18*, 396–410. https://doi.org/10.1093/emboj/18.2.396.

40. Saha, P., Chen, J., Thome, K.C., Lawlis, S.J., Hou, Z.H., Hendricks, M., Parvin, J.D., and Dutta, A. (1998). Human CDC6/Cdc18 associates with Orc1 and cyclin-cdk and is selectively eliminated from the nucleus at the onset of S phase. Mol. Cell Biol. *18*, 2758–2767. https://doi.org/10.1128/mcb.18.5.2758.

41. Au-Yeung, G., Lang, F., Azar, W.J., Mitchell, C., Jarman, K.E., Lackovic, K., Aziz, D., Cullinane, C., Pearson, R.B., Mileshkin, L., et al. (2017). Selective Targeting of Cyclin E1-Amplified High-Grade Serous Ovarian Cancer by Cyclin-Dependent Kinase 2 and AKT Inhibition. Clin. Cancer Res. *23*, 1862–1874. https://doi.org/10.1158/1078-0432.CCR-16-0620.

42. Chi, Y., Welcker, M., Hizli, A.A., Posakony, J.J., Aebersold, R., and Clurman, B.E. (2008). Identification of CDK2 substrates in human cell lysates. Genome Biol. *9*, R149. https://doi.org/10.1186/gb-2008-9-10-r149.

43. Sarcevic, B., Lilischkis, R., and Sutherland, R.L. (1997). Differential Phosphorylation of T-47D Human Breast Cancer Cell Substrates by D1-D3-E- and A-type Cyclin-CDK Complexes. J. Biol. Chem. *272*, 33327–33337. https://doi.org/10.1074/jbc.272.52.33327.

44. Akiyama, T., Ohuchi, T., Sumida, S., Matsumoto, K., and Toyoshima, K. (1992). Phosphorylation of the retinoblastoma protein by cdk2. Proc. Natl. Acad. Sci. USA *89*, 7900–7904.

45. Tetsu, O., and McCormick, F. (2003). Proliferation of cancer cells despite CDK2 inhibition. Cancer Cell *3*, 233–245. https://doi.org/10.1016/s1535-6108(03)00053-9.

46. Lundberg, A.S., and Weinberg, R.A. (1998). Functional Inactivation of the Retinoblastoma Protein Requires Sequential Modification by at Least Two Distinct Cyclin-cdk Complexes. Mol. Cell Biol. *18*, 753–761. https://doi.org/10.1128/MCB.18.2.753.

47. Guarducci, C., Bonechi, M., Benelli, M., Biagioni, C., Boccalini, G., Romagnoli, D., Verardo, R., Schiff, R., Osborne, C.K., De Angelis, C., et al. (2018). Cyclin E1 and Rb modulation as common events at time of resistance to palbociclib in hormone receptor-positive breast cancer. npj Breast Cancer *4*, 38. https://doi.org/10.1038/s41523-018-0092-4.

48. Fry, D.W., Harvey, P.J., Keller, P.R., Elliott, W.L., Meade, M., Trachet, E., Albassam, M., Zheng, X., Leopold, W.R., Pryer, N.K., and Toogood, P.L. (2004). Specific inhibition of cyclin-dependent kinase 4/6 by PD 0332991 and associated antitumor activity in human tumor xenografts.

Mol. Cancer Ther. *3*, 1427–1438. https://doi.org/10.1158/1535-7163.1427.3.11.

49. Ma, Y., Kurtyka, C.A., Boyapalle, S., Sung, S.-S., Lawrence, H., Guida, W., and Cress, W.D. (2008). A Small-Molecule E2F Inhibitor Blocks Growth in a Melanoma Culture Model. Cancer Res. *68*, 6292–6299. https://doi.org/10.1158/0008-5472.CAN-08-0121.

50. Hégarat, N., Crncec, A., Suarez Peredo Rodriguez, M.F., Echegaray Iturra, F., Gu, Y., Busby, O., Lang, P.F., Barr, A.R., Bakal, C., Kanemaki, M.T., et al. (2020). Cyclin A triggers Mitosis either via the Greatwall kinase pathway or Cyclin B. EMBO J. *39*, e104419. https://doi.org/10.15252/embj.2020104419.

51. Collin, P., Nashchekina, O., Walker, R., and Pines, J. (2013). The spindle assembly checkpoint works like a rheostat rather than a toggle switch. Nat. Cell Biol. *15*, 1378–1385. https://doi.org/10.1038/ncb2855.

52. Merrick, K.A., Wohlbold, L., Zhang, C., Allen, J.J., Horiuchi, D., Huskey, N.E., Goga, A., Shokat, K.M., and Fisher, R.P. (2011). Switching Cdk2 on or off with small molecules to reveal requirements in human cell proliferation. Mol. Cell *42*, 624–636. https://doi.org/10.1016/j.molcel.2011.03.031.

53. Frame, S., Saladino, C., MacKay, C., Atrash, B., Sheldrake, P., McDonald, E., Clarke, P.A., Workman, P., Blake, D., and Zheleva, D. (2020). Fadraciclib (CYC065), a novel CDK inhibitor, targets key pro-survival and oncogenic pathways in cancer. PLoS One *15*, e0234103. https://doi.org/10.1371/journal.pone.0234103.

54. Rana, S., Mallareddy, J.R., Singh, S., Boghean, L., and Natarajan, A. (2021). Inhibitors, PROTACs and Molecular Glues as Diverse Therapeutic Modalities to Target Cyclin-Dependent Kinase. Cancers *13*, 5506. https://doi.org/10.3390/cancers13215506.

55. Mezi, S., Botticelli, A., Pomati, G., Cerbelli, B., Scagnoli, S., Amirhassankhani, S., d'Amati, G., and Marchetti, P. (2021). Standard of Care and Promising New Agents for the Treatment of Mesenchymal Triple-Negative Breast Cancer. Cancers *13*, 1080. https://doi.org/10.3390/cancers13051080.

56. Fassl, A., Geng, Y., and Sicinski, P. (2022). CDK4 and CDK6 kinases: From basic science to cancer therapy. Science *375*, eabc1495. https://doi.org/10.1126/science.abc1495.

57. Jhaveri, K., Burris Rd, H.A., Yap, T.A., Hamilton, E., Rugo, H.S., Goldman, J.W., Dann, S., Liu, F., Wong, G.Y., Krupka, H., and Shapiro, G.I. (2021). The evolution of cyclin dependent kinase inhibitors in the treatment of cancer. Expert Rev. Anticancer Ther. *21*, 1105–1124. https://doi.org/10.1080/14737140.2021.1944109.

58. Hoffman, R.L. (2021). The discovery of PF-07104091: A CDK2 selective inhibitor for the treatment of cyclin E amplified cancers. AACR Annual Meeting.

59. Bártová, I., Otyepka, M., Kríz, Z., and Koča, J. (2004). Activation and inhibition of cyclin-dependent kinase-2 by phosphorylation; a molecular dynamics study reveals the functional importance of the glycine-rich loop. Protein Sci. *13*, 1449–1457. https://doi.org/10.1110/ps.03578504.

60. Desai, D., Gu, Y., and Morgan, D.O. (1992). Activation of human cyclin-dependent kinases in vitro. MBoC *3*, 571–582. https://doi.org/10.1091/mbc.3.5.571.

61. Witkiewicz, A.K., Kumarasamy, V., Sanidas, I., and Knudsen, E.S. (2022). Cancer cell cycle dystopia: heterogeneity, plasticity, and therapy. Trends Cancer *8*, 711–725. https://doi.org/10.1016/j.trecan.2022.04.006.

62. Basu, S., Greenwood, J., Jones, A.W., and Nurse, P. (2022). Core control principles of the eukaryotic cell cycle. Nature *607*, 381–386. https://doi.org/10.1038/s41586-022-04798-8.

63. Wood, D.J., and Endicott, J.A. (2018). Structural insights into the functional diversity of the CDK–cyclin family. Open Biol. *8*, 180112. https://doi.org/10.1098/rsob.180112.

64. Schwarz, C., Johnson, A., Kõivomägi, M., Zatulovskiy, E., Kravitz, C.J., Doncic, A., and Skotheim, J.M. (2018). A Precise Cdk Activity Threshold Determines Passage through the Restriction Point. Mol. Cell *69*, 253–264.e5. https://doi.org/10.1016/j.molcel.2017.12.017.

65. Tambo, C.S., Tripathi, S., Perera, B.G.K., Maly, D.J., Bridges, A.J., Kiss, G., and Rubin, S.M. (2023). Biolayer Interferometry Assay for Cyclin-Dependent Kinase-Cyclin Association Reveals Diverse Effects of Cdk2 Inhibitors on Cyclin Binding Kinetics. ACS Chem. Biol. *18*, 431–440. https://doi.org/10.1021/acschembio.3c00015.

66. Chellappan, S.P., Hiebert, S., Mudryj, M., Horowitz, J.M., and Nevins, J.R. (1991). The E2F transcription factor is a cellular target for the RB protein. Cell *65*, 1053–1061. https://doi.org/10.1016/0092-8674(91)90557-f.

67. Fassl, A., Brain, C., Abu-Remaileh, M., Stukan, I., Butter, D., Stepien, P., Feit, A.S., Bergholz, J., Michowski, W., Otto, T., et al. (2020). Increased lysosomal biomass is responsible for the resistance of triple-negative breast cancers to CDK4/6 inhibition. Sci. Adv. *6*, eabb2210. https://doi.org/10.1126/sciadv.abb2210.

68. Prevo, R., Pirovano, G., Puliyadi, R., Herbert, K.J., Rodriguez-Berriguete, G., O'Docherty, A., Greaves, W., McKenna, W.G., and Higgins, G.S. (2018). CDK1 inhibition sensitizes normal cells to DNA damage in a cell cycle dependent manner. Cell Cycle *17*, 1513–1523. https://doi.org/10.1080/15384101.2018.1491236.

69. Li, Q., Jiang, B., Guo, J., Shao, H., Del Priore, I.S., Chang, Q., Kudo, R., Li, Z., Razavi, P., Liu, B., et al. (2022). INK4 Tumor Suppressor Proteins Mediate Resistance to CDK4/6 Kinase Inhibitors. Cancer Discov. *12*, 356–371. https://doi.org/10.1158/2159-8290.CD-20-1726.

70. Guiley, K.Z., Stevenson, J.W., Lou, K., Barkovich, K.J., Kumarasamy, V., Wijeratne, T.U., Bunch, K.L., Tripathi, S., Knudsen, E.S., Witkiewicz, A.K., et al. (2019). p27 allosterically activates cyclin-dependent kinase 4 and antagonizes palbociclib inhibition. Science *366*, eaaw2106. https://doi.org/10.1126/science.aaw2106.

71. Liu, J.C., Granieri, L., Shrestha, M., Wang, D.-Y., Vorobieva, I., Rubie, E.A., Jones, R., Ju, Y., Pellecchia, G., Jiang, Z., et al. (2018). Identification of CDC25 as a Common Therapeutic Target for Triple-Negative Breast Cancer. Cell Rep. *23*, 112–126. https://doi.org/10.1016/j.celrep.2018.03.039.

72. Gallo, D., Young, J.T.F., Fourtounis, J., Martino, G., Álvarez-Quilón, A., Bernier, C., Duffy, N.M., Papp, R., Roulston, A., Stocco, R., et al. (2022). CCNE1 amplification is synthetic lethal with PKMYT1 kinase inhibition. Nature *604*, 749–756. https://doi.org/10.1038/s41586-022-04638-9.

73. Jonkers, J., Meuwissen, R., van der Gulden, H., Peterse, H., van der Valk, M., and Berns, A. (2001). Synergistic tumor suppressor activity of BRCA2 and p53 in a conditional mouse model for breast cancer. Nat. Genet. *29*, 418–425. https://doi.org/10.1038/ng747.

74. Guerra, C., Mijimolle, N., Dhawahir, A., Dubus, P., Barradas, M., Serrano, M., Campuzano, V., and Barbacid, M. (2003). Tumor induction by an endogenous K-ras oncogene is highly dependent on cellular context. Cancer Cell *4*, 111–120. https://doi.org/10.1016/s1535-6108(03)00191-0.

75. Yang, C., Tian, C., Hoffman, T.E., Jacobsen, N.K., and Spencer, S.L. (2021). Melanoma subpopulations that rapidly escape MAPK pathway inhibition incur DNA damage and rely on stress signalling. Nat. Commun. *12*, 1747.

76. Dull, T., Zufferey, R., Kelly, M., Mandel, R.J., Nguyen, M., Trono, D., and Naldini, L. (1998). A Third-Generation Lentivirus Vector with a Conditional Packaging System. J. Virol. *72*, 8463–8471. https://doi.org/10.1128/JVI.72.11.8463-8471.1998.

77. Stewart, S.A., Dykxhoorn, D.M., Palliser, D., Mizuno, H., Yu, E.Y., An, D.S., Sabatini, D.M., Chen, I.S.Y., Hahn, W.C., Sharp, P.A., et al. (2003). Lentivirus-delivered stable gene silencing by RNAi in primary cells. RNA *9*, 493–501. https://doi.org/10.1261/rna.2192803.

78. Cappell, S.D., Chung, M., Jaimovich, A., Spencer, S.L., and Meyer, T. (2016). Irreversible APCCdh1 Inactivation Underlies the Point of No Return

for Cell-Cycle Entry. Cell *166*, 167–180. https://doi.org/10.1016/j.cell.2016.05.077.

79. Lee, C.-L., Moding, E.J., Huang, X., Li, Y., Woodlief, L.Z., Rodrigues, R.C., Ma, Y., and Kirsch, D.G. (2012). Generation of primary tumors with Flp recombinase in FRT-flanked p53 mice. Dis. Model. Mech. *5*, 397–402. https://doi.org/10.1242/dmm.009084.

80. Lapek, J.D., Lewinski, M.K., Wozniak, J.M., Guatelli, J., and Gonzalez, D.J. (2017). Quantitative Temporal Viromics of an Inducible HIV-1 Model Yields Insight to Global Host Targets and Phospho-Dynamics Associated with Protein Vpr. Mol. Cell. Proteomics *16*, 1447–1461. https://doi.org/10.1074/mcp.M116.066019.

81. Lapek, J.D., Greninger, P., Morris, R., Amzallag, A., Pruteanu-Malinici, I., Benes, C.H., and Haas, W. (2017). Detection of dysregulated protein-association networks by high-throughput proteomics predicts cancer vulnerabilities. Nat. Biotechnol. *35*, 983–989. https://doi.org/10.1038/nbt.3955.

82. Edwards, A., and Haas, W. (2016). Multiplexed Quantitative Proteomics for High-Throughput Comprehensive Proteome Comparisons of Human Cell Lines. In Proteomis in Systems Biology Methods in Molecular Biology (Springer) https://doi.org/10.1007/978-1-4939-3341-9.

83. Xu, T., Park, S.K., Venable, J.D., Wohlschlegel, J.A., Diedrich, J.K., Cociorva, D., Lu, B., Liao, L., Hewel, J., Han, X., et al. (2015). ProLuCID: An improved SEQUEST-like algorithm with enhanced sensitivity and specificity. J. Proteomics *129*, 16–24. https://doi.org/10.1016/j.jprot.2015.07.001.

84. Huttlin, E.L., Jedrychowski, M.P., Elias, J.E., Goswami, T., Rad, R., Beausoleil, S.A., Villén, J., Haas, W., Sowa, M.E., and Gygi, S.P. (2010). A Tissue-Specific Atlas of Mouse Protein Phosphorylation and Expression. Cell *143*, 1174–1189. https://doi.org/10.1016/j.cell.2010.12.001.

85. Arora, M., Moser, J., Phadke, H., Basha, A.A., and Spencer, S.L. (2017). Endogenous Replication Stress in Mother Cells Leads to Quiescence of Daughter Cells. Cell Rep. *19*, 1351–1364. https://doi.org/10.1016/j.celrep.2017.04.055.

86. Evron, E., Umbricht, C.B., Korz, D., Raman, V., Loeb, D.M., Niranjan, B., Buluwela, L., Weitzman, S.A., Marks, J., and Sukumar, S. (2001). Loss of cyclin D2 expression in the majority of breast cancers is associated with promoter hypermethylation. Cancer Res. *61*, 2782–2787.

STAR★METHODS

KEY RESOURCES TABLE

Reagent or resource	SOURCE	IDENTIFIER
Antibodies		
Rb	Cell Signaling Technology	Cat# 9309; RRID: AB_823629
phospho-Rb (S807/811)	Cell Signaling Technology	Cat# 8516; RRID: AB_11178658
NCL	Abcam	Cat# ab13541; RRID: AB_300442
phospho-NCL (T84)	Abcam	Cat# ab155977
p21	Santa Cruz	Cat# sc-6246; RRID: AB_628073
phospho-NBS1 (S343)	Thermo Fisher Scientific	Cat# PA5-78070; RRID: AB_2736393
phospho-CDC6 (S54)	Abcam	Cat# ab75809; RRID: AB_1310068
GAPDH (in Figures S3 and S4)	Cell Signaling Technology	Cat# 5174; RRID: AB_10622025
GAPDH (in Figure 7)	Invitrogen	Cat# ZG003
Vinculin	Sigma Aldrich	Cat# V9131; RRID: AB_477629
β-tubulin	Cell Signaling Technology	Cat# 86298; RRID: AB_2715541
Histone H3	Cell Signaling Technology	Cat# 3638; RRID: AB_1642229
CDK1	Abcam	Cat# ab133327; RRID: AB_11155333
CDK2 (for IP)	Santa Cruz	Cat# sc-6248; RRID: AB_627238
CDK2 (for blotting)	Abcam	Cat# ab32147; RRID: AB_726775
CDK4	Abcam	Cat# ab108357; RRID: AB_10867218
CDK6	Abcam	Cat# ab151247
Cyclin D1	Abcam	Cat# ab134175; RRID: AB_2750906
Cyclin D2	Cell Signaling Technology	Cat# 3741; RRID: AB_2070685
Cyclin D3	Cell Signaling Technology	Cat# 2936; RRID: AB_2070801
Cyclin E1 (EP435E) (for IF imaging and IP)	Abcam	Cat# ab33911; RRID: AB_731787
Cyclin E2 (EP454Y) (for IF imaging)	Abcam	Cat# ab40890; RRID: AB_2071187
Cyclin E (for blotting)	Santa Cruz	Cat# sc-377100; RRID: AB_2923122
Cyclin A2 (for IF)	Santa Cruz	Cat# sc-751; RRID: AB_631329
Cyclin A2 (for IF and blotting)	Santa Cruz	Cat# sc-271682; RRID: AB_10709300
E2F1	Santa Cruz	Cat# sc-251; RRID: AB_627476
phospho-CDK2 (T160)	Cell Signaling Technology	Cat# 2561; RRID: AB_2078685
Alexa Fluor 488 goat anti-mouse	Thermo Fisher Scientific	Cat# A-11001
Alexa Fluor 546 goat anti-rabbit	Thermo Fisher Scientific	Cat# A-11035
Alexa Fluor 647 secondary	Thermo Fisher Scientific	Cat# A21245, A21236
Alexa Fluor 680 secondary	Invitrogen	Cat# A27042, A28183
HRP-linked anti-mouse	Cell Signaling Technology	Cat# 7076
HRP-linked anti-rabbit	Cell Signaling Technology	Cat# 7074
Chemicals, peptides, and recombinant proteins		
PF3600	Pfizer Inc.	CAS: 2185857-97-8
Palbociclib	Pfizer Inc.	CAS: 571190-30-2
RO3306	SelleckChem	Cat# S7747
Ribociclib	MedChemExpress	Cat# HY-15777
Abemaciclib	MedChemExpress	Cat# HY-16297A
Fadraciclib	MedChemExpress	Cat# HY-101212
CVT-313	EMD Millipore	Cat# 238803
E2F inhibitor	Sigma Aldrich	Cat# 324461
PF-07104091	ChemiTek	Cat# CT-PF0710
Doxycycline	Sigma Aldrich	Cat# D9891

(*Continued on next page*)

Continued

Reagent or resource	SOURCE	IDENTIFIER
Indole-3-acetic acid	Sigma Aldrich	Cat# I5148
3MB-PP1	Cayman Chemical	Cat# 17860
Critical commercial assays		
ViewRNA ISH Kit	Thermo Fisher Scientific	Cat# QVC001
Annexin V-FITC Apoptosis Kit	Abcam	Cat# ab14085
Lipofectamine™ CRISPRMAX™	Thermo Fisher Scientific	Cat# CMAX00003
Neon Transfection System Kit	Thermo Fisher Scientific	Cat# MPK10096
Click-iT EdU Imaging Kit	Thermo Fisher Scientific	Cat# C10340
BCA Protein Assay Kit	Pierce	Cat# 23227
Deposited data		
Phospho-proteomic dataset	This paper	MassIVE: MSV000091849; ProteomeXchange Consortium: PXD041959
Experimental models: Human cell lines		
MCF10A	ATCC	Cat# CRL-10317, RRID: CVCL_0598
RPE-hTERT	ATCC	Cat# CRL-4000
MCF7	ATCC	Cat# HTB-22
OVCAR3	ATCC	Cat# HTB-161, RRID: CVCL_0465
MCF10A (DHB-mVenus, H2B-mTurq2)	Spencer et al. (2013)[12]	N/A
MCF10A (CDC6-YFP, DHB-mCherry, H2B-mTurq2)	This paper	N/A
MCF7 (DHB-mCherry, H2B-mTurq2)	This paper	N/A
RPE-hTERT (DHB-mVenus, H2B-mTurq2)	This paper	N/A
OVCAR3 (DHB-mVenus, H2B-mTurq2)	This paper	N/A
MCF10A (PF3600R)	This paper	N/A
MCF10A (Rb1-KO)	This paper	N/A
MCF10A (Rb1-KO) (DHB-mVenus, H2B-mTurq2)	This paper	N/A
RPE-hTERT ($CycA^{dd}$) (CDK2 sensor added)	Hégarat et al. 2020[50]	N/A
RPE-hTERT (CycA2-mVenus) (CDK2 sensor added)	Collin et al. 2013[51]	N/A
RPE-hTERT ($CDK2^{F80G/F80G}$) (CDK2 sensor added)	Merrick et al. 2011[52]	N/A
Experimental models: Organisms/strains		
C57BL/6 mice ($Kras^{+/LSLG12V}$; $Trp53^{L/L}$, $Cdk2^{WT}$)	Ortega et al. 2003[19] Jonkers et al. 2001[73] Guerra et al. 2003[74]	N/A
C57BL/6 mice ($Kras^{+/LSLG12V}$; $Trp53^{L/L}$, $Cdk2^{-/-}$)	Ortega et al. 2003[19] Jonkers et al. 2001[73] Guerra et al. 2003[74]	N/A
Oligonucleotides		
GTTCGAGGTGAACCATTAAT (RB1 crRNA)	Integrated DNA Technologies	Cat# Hs.Cas9.RB1.1.AA
siCCND1	Dharmacon	Cat# MU-003210-05-0005
siCCND2	Dharmacon	Cat# MU-003211-02-0005
siCCND3 #1	Dharmacon	Cat# J-003212-10-0002
siCCND3 #2	Dharmacon	Cat# J-003212-11-0002
siCCND3 #3	Dharmacon	Cat# J-003212-12-0002
siCDK4 #1	Integrated DNA Technologies	Cat# 198569326
siCDK4 #2	Integrated DNA Technologies	Cat# 198569329
siCDK4 #3	Integrated DNA Technologies	Cat# 198569332
siCDK6 #1	Integrated DNA Technologies	Cat# 200925870

(*Continued on next page*)

Continued

Reagent or resource	SOURCE	IDENTIFIER
siCDK6 #2	Integrated DNA Technologies	Cat# 200925873
siCDK6 #3	Integrated DNA Technologies	Cat# 200925876
siRB1 #1	Integrated DNA Technologies	Cat# hs.Ri.RB1.13.1
siRB1 #2	Integrated DNA Technologies	Cat# hs.Ri.RB1.13.2
siCCNE1	Dharmacon	Cat# M-003213-02-0005
siCCNE2	Dharmacon	Cat# M-003214-02-0005
siCCNA2	Dharmacon	Cat# M-003205-02-0005
E2F1 FISH probe	Thermo Fisher Scientific	Cat# VA6-3168356-VC
CCNA2 FISH probe	Thermo Fisher Scientific	Cat# VA6-15304
CCNE1 FISH probe	Thermo Fisher Scientific	Cat# VA6-3167995
Recombinant DNA		
CSII-EF DHB-mVenus	Meyer Lab; Spencer Lab[12]	Addgene Cat# 136461
CSII-EF DHB-mCherry	Meyer Lab; Spencer Lab[12]	N/A
CSII-EF CDC6-YFP	This paper	N/A
CSII-EF H2B-mTurquoise	Meyer Lab; Spencer Lab[12]	N/A
CSII-EF H2B-mCherry	Meyer Lab; Spencer Lab[12]	N/A
CSII-EF H2B-miFP	Spencer Lab[75]	N/A
pMDLg	Dull et al. 1998[76]	Addgene Cat# 12251
pRSV-Rev	Dull et al. 1998[76]	Addgene Cat# 12253
pCMV-VSV-G	Stewart et al. 2003[77]	Addgene Cat# 8454
Software and algorithms		
MATLAB	MathWorks	https://www.mathworks.com/products/matlab.html
Fiji (ImageJ)	Cardona Lab	https://imagej.net/software/fiji/
Harmony	PerkinElmer	https://www.perkinelmer.com/uk/product/harmony-4-6-office-hh17000001
GraphPad Prism	GraphPad	https://www.graphpad.com/features
Cell-tracking pipeline	Meyer Lab	Cappell et al.[78] https://github.com/scappell/Cell_tracking
Immunofluorescence image processing and analysis	Meyer Lab; Spencer Lab	https://github.com/tiho9814/matlab_image_processing_scripts/tree/main/scripts_IF https://doi.org/10.5281/zenodo.7860489
Analysis scripts for plotting tracedata mat files	Spencer Lab	https://github.com/tiho9814/matlab_image_processing_scripts/tree/main/scripts_tracedata_plotting https://doi.org/10.5281/zenodo.7860489

RESOURCE AVAILABILITY

Lead contact

Further information and requests for resources and reagents should be directed to and will be fulfilled by the lead contact, Sabrina Spencer (sabrina.spencer@colorado.edu).

Materials availability

Raw data, cell lines, and materials are available from the lead contact upon reasonable request.

Data and code availability

The phospho-proteomics dataset is available as Table S2 and in both MassIVE and the ProteomeXchange Consortium (MSV000091849/PXD041959) repositories. Cell-tracking scripts and analysis code are available in GitHub (https://doi.org/10.5281/zenodo.7860489; see key resources table). Any additional information required to reanalyze the data reported in this paper is available from the lead contact upon request.

EXPERIMENTAL MODEL AND SUBJECT DETAILS

Cell culture

Cell lines used in this study were primarily obtained from ATCC. In Figure 6H, RPE hTERT CycA2-mVenus cells were courtesy of Jörg Mansfeld at the Institute of Cancer Research, London, UK.[51] In Figure 6G, RPE-hTERT CyclinA^{dd} cells were courtesy of Helfrid Hochegger at the University of Sussex, Brighton, UK. In Figures 7A and S7A–S7C, wild-type and CDK2 analog sensitive cells were courtesy of Robert Fisher at the Icahn School of Medicine, New York, US. MCF10A (human breast epithelial) cells were cultured in DMEM/F12 supplemented with 5% horse serum (Invitrogen), 20 ng/mL (Sigma-Aldrich), 0.5 mg/mL hydrocortisone (Sigma-Aldrich), 100 ng/mL cholera toxin (Sigma-Aldrich), and 10 μg/mL insulin (Invitrogen). RPE-hTERT cells were grown in DMEM with 10% FBS and 1X GlutaMAX. MCF7 and OVCAR3 cells were grown using RPMI-1640 supplemented with 10% FBS. Except during siRNA transfections, all full-growth media were supplemented with Penicillin/Streptomycin. All cells were cultured at 37°C with 5% CO_2. MCF10A-PF3600R cells were generated by continuous culture of MCF10A WT cells in 100 nM PF3600 for 1 month (refreshed drug every 3 days), and cells were immediately harvested for dose-response profiling with no drug holiday.

Stable cell line generation using lentiviral vectors

Cells stably expressing fluorescent proteins were generated by lentivirus transduction. For virus generation, HEK293T or HEK293FT cells were transfected with CSII-EF plasmid (CSII-EF DHB-mVenus, CSII-EF DHB-mCherry, CSII-EF CDC6-YFP, CSII-EF H2B-mTurquoise, CSII-EF H2B-mCherry, or CSII-EF H2B-mIFP) along with the helper packaging and envelope plasmids (pMDLg, pRSV-Rev, pCMV-VSV-G) using the Fugene-HD reagent (Promega E2311). Lentivirus was harvested 48 h after transfection, filtered through a 0.45 μm filter (Millipore), and incubated with target cells for 6–10 h in presence of 5 μg/mL polybrene (EMD Millipore #TR-1003). Cells with stable integrations were sorted on an Aria Fusion Flow Cytometer to establish a population where all cells express the desired sensors.

RB1 knockout cell line generation

RB1 knockout MCF10A cells were generated using the Alt-R CRISPR-Cas9 system from Integrated DNA Technologies (IDT) following the manufacturer's protocol using a predesigned crRNA that targets one site near the 5′-end of the RB1 coding sequence: GTTCGAGGTGAACCATTAAT (IDT design ID: Hs.Cas9.RB1.1.AA). The ribonucleoprotein (RNP) contains crRNA annealed to a universal tracrRNA (crRNA:tracrRNA duplex or sgRNA) and purified Cas9 nuclease. The RNP was delivered into MCF10A cells using the Lipofectamine CRISPRMAX reagent (Thermo Fisher Scientific) following the manufacturer's protocol. Single RB1 knockout MCF10A cells were seeded into 96 well plates by serial dilution to obtain clonal knockout cells. Western blot against total Rb was carried out as validation.

Mouse studies

Genetically engineered mice harboring the following alleles: Kras$^{+/LSLG12V}$; Trp53$^{L/L}$ and Cdk2$^{-/-}$ were used in this study.[19,73,74] Mice were kept on a homogeneous mixed background and both genders were used.

Compound mice using the following transgenes: *Kras*$^{+/LSLG12V}$[74]; *Trp53*$^{L/L}$,[79] and *Cdk2*$^{-/-}$[19] were readily available for this study, appropriate to test the efficacy of co-inhibiting CDK activities. All animal experiments were approved by the Ethical Committees of the Spanish National Cancer Research Centre (CNIO), the Carlos III Health Institute and the Autonomous Community of Madrid (PROEX 270/14) and were performed in accordance with the guidelines stated in the International Guiding Principles for Biomedical Research Involving Animals, developed by the Council for International Organizations of Medical Sciences (CIOMS). Mice were housed in specific-pathogen-free conditions at CNIO's Animal Facility (AAALAC, JRS:dpR 001659). All mice were genotyped at the CNIO's Genomic Unit.

Cohort sizes

The mice were randomly put in treatment groups based on the following criteria: (1) Each group was designed to contain similar or equal number of mice; (2) Each group was designed to possesses similar or equal number of tumors in total among all the animals; (3) Each treatment was designed to contain similar sizes of tumors at the beginning of the treatment. The numbers of mice included in this study are: CDK2 WT (Vehicle: mice = 9, tumors = 14; PF3600: mice = 10, tumors = 52) and CDK2 KO (Vehicle: mice = 11, tumors = 31; Palbociclib: mice = 13, tumors = 45).

Lung tumor induction

Induction of lung adenocarcinomas was carried out in anesthetized (ketamine 75 mg/kg, xylazine 12 mg/kg) 8-week old mice by intranasal instillation of a single dose of 10^6 pfu/mouse of adeno viruses encoding the Cre recombinase (Ad-Cre). All the adenoviral preparations were purchased from the University of Iowa (Iowa City, USA).

Micro CT imaging

Image studies were done by the Molecular Imaging Core Unit at the CNIO. Mice were anesthetized with a continuous flow of 1% to 3% isoflurane/oxygen mixture (0.5 L/min) and the chest area was imaged by three-dimensional microcomputed tomography performed with a CompaCT scanner (SEDECAL Madrid SpainGE). Data were acquired with 720 projections by 360-degree scan, integration time of 100 ms with three frames, photon energy of 50 KeV, and current of 100 μA. Tumor measurements were obtained with GE MicroView software v2.2. Tumor volume was calculated as follows: (short axis x short axis x long axis/2).

Pharmacological treatment in mice

8 month old *Kras*$^{+/LSLG12V}$;*Trp53*$^{L/L}$;*Cdk2*$^{-/-}$ and *Kras*$^{+/LSLG12V}$;*Trp53*$^{L/L}$;*Cdk2*$^{+/+}$ mice were infected with 10^6 pfu of Ad-Cre. Once tumors were detected by CT, mice harboring at least one tumor bigger than 3 mm^3 were enrolled in the different treatment groups. Palbociclib was dosed at 70 mg/kg QD for 4 weeks and PF3600 was dosed at 50 mg/kg BID for 4 weeks. Drug efficacy was monitored by CT measurements.

METHOD DETAILS

siRNA transfections

siRNA transfections were carried out with the Dharmafect1 reagent (https://horizondiscovery.com/-/media/Files/Horizon/resources/Quick-protocols/dharmafect-rna-transfection-quick-protocol.pdf). Briefly, cells were seeded in 96-well plates and transfection mixtures were prepared in order to deliver 100 μL per well. Transfection mixtures contained a final total siRNA concentration of 25 nM and a final Dharmafect1 concentration of 0.25% (v/v). Adherent cells were incubated with the transfection mixture for 6 h in antibiotic-free media, which was subsequently washed off and replaced with full-growth media containing treatments of interest. See key resources table for detailed identifiers for each target sequence.

Time-lapse imaging

Cells were seeded at least 24 h prior to imaging in phenol-red-free full-growth medium in glass-bottom 96-well plates (CellVis P96-1.5H-N) that were coated with collagen prior to seeding. The seeding density was chosen such that the cells would remain sub-confluent until the end of the imaging period. Cells were first imaged for 16–20 h in full-growth media without drug. The movie was then briefly paused, and the full-growth media was replaced with full-growth media containing drug at the desired concentration. The plate was then re-inserted into the microscope and aligned to its prior position and imaging was continued for an additional 24–48 h. For the Cyclin A2^{dd} RPE-hTERT cell line, cells were seeded and imaged as described, but cells were dosed with DIA (doxycycline and indole-3-acetic-acid) 2 h before the addition of PF3600. For time-lapse experiments involving siRNA knockdown of CDKs, imaging was started immediately following siRNA transfections. Media was changed 6 h after transfection, and imaging was continued for 14 h in absence of drug. PF3600 (or DMSO) was then added (at 20 h post transfection) and cells were imaged for an additional 24 h. For siRNA knockdown of cyclins, cells were first imaged in full-growth medium for 20h. The transfection complexes were added for 6h, at which point the media was replaced with media containing DMSO or PF3600 and imaging was carried out for an additional 24 h. For siRNA knockdown of Rb1, cells were electroporated with the indicated nontargeting or targeted siRNA using the Neon Transfection System (Thermo Fisher) and seeded immediately. 24 h after seeding, cells were imaged for 16 h, after which DMSO or the indicated drugs were added and cells were imaged for an additional 14 h, after which they were fixed and probed for mRNA or protein. Images were acquired every 12 min (for MCF10A and OVCAR3) or every 20 min (for MCF7 or RPE-hTERT) on a Nikon Eclipse Ti or Ti2 microscope with a 10X 0.45 NA objective in a humidified, 37°C chamber at 5% CO_2. Exposure times for all movies for all channels were kept under 500 ms per timepoint to minimize phototoxicity.

Immunofluorescence

Cells were fixed for 15 min with freshly prepared 4% paraformaldehyde, washed twice with PBS, and incubated with a blocking buffer (3% BSA in PBS) for 1 h at room temperature. Permeabilization was carried out using 0.2% Triton X-100 for 15 min at 4°C. For samples stained for EdU incorporation, the manufacturer's protocol was followed prior to immunostaining (Thermo Fisher, C10340). Primary antibody was diluted in blocking buffer and incubated with cells overnight at 4°C followed by three washes with 1X PBS. Secondary antibodies conjugated to Alexa Fluor 488, Alexa Fluor 546 or Alexa Fluor 647 were incubated for 1 h followed by three washes with 1X PBS. DNA was stained using Hoechst 33342 dye for 10 min at 1:10000 (Thermo Fisher, H3570). Images were acquired on a Nikon Eclipse Ti or Ti2 microscope with a 10X 0.45 NA objective. DNA content was determined by taking the integrated intensity of each cell's Hoechst signal. Cells were delineated as 3-4N DNA content by plotting a histogram of DNA content and drawing a threshold and the end of the 2N peak. In Figures 4, S4, and S7, the vertical gates used to isolate S phase cells were automatically set by using Otsu's method to identify the midpoint between the 2N and 4N populations, which was then extended by 15% on either side to approximate the S phase population.

Apoptosis assay

Cells were seeded in 12-well plates (Corning, #3513), at 10^5 cells/well, 24 h prior to drug treatments. Wells were treated in triplicate with indicated drugs for 24, 48, or 72h. After treatment, non-adherent cells were first harvested by pipetting, adherent cells were harvested by trypsinization, and these two populations were then combined. Cell suspensions were centrifuged and resuspended in calcium-rich binding buffer provided by the apoptosis staining kit (abcam, #ab14085) to reach ~10^6 cells/mL. Live suspensions were stained with both Annexin V-FITC (1:100) and propidium iodide, PI (1:100). Single-cell fluorescent signals were acquired on a BD FACSCelesta flow cytometer equipped with 488 and 561 nm lasers.

Long-term treatment experiment

MCF10A cells expressing the nuclear marker H2B-mTurquoise and CDK2 activity sensory DHB-mVenus were seeded in a Poly-D lysine-coated 96-well PhenoPlate (PerkinElmer 6055500) at 1,000 cells per well and treated with the indicated drugs the following day and imaged (day 0). Each condition consisted of six replicate wells and the entire well was imaged. Treatments were refreshed and cells (H2B-mTurquoise signal) were imaged with a 5X objective on an Opera Phenix (PerkinElmer) on days 0, 1, 2, 3, 7, 10, 14, 17, 21, 24, 28, 31, 35 and 38. To quantify the number of cells, nuclear segmentation of the H2B signal was performed using the Harmony software (PerkinElmer).

7-day treatment experiment

MCF10A and MCF7 cells expressing the nuclear marker H2B-mTurquoise and CDK2 activity sensor (DHB-mVenus or DHB-mCherry, respectively) were seeded in a collagen-treated 96-well plate at 3,500 cells per well and treated with the indicated drugs the following day. Treatments were refreshed at 72 h. Each condition consisted of four replicate wells, and each well was imaged at four individual sites. At hours 0, 24, 48, 72, 96, and 120, static images were taken to assess the change in cell count. Between hours 144 and 168, time-lapse imaging was performed on the same well sites to visualize dynamic CDK2 activity and mitotic events during extended treatment as well as change in cell count. Control MCF10A cells became contact inhibited by day 3. As non-contact-inhibited controls for the movie, fresh untreated cells were seeded into empty collagen-treated wells 24 h prior to the start of the time-lapse imaging period. The static images for hours 0, 24, 48, 72, 96, and 120, along with the individual movie frames for hours 144 and 168, were all subject to nuclear segmentation of the H2B signal via MATLAB scripts (see key resources table) to quantify the number of cells in the field of view, which are expressed as the fold change in cell count relative to day 0. The number of mitoses that occurred for each treatment condition between hours 144–168 in the movie were automatically detected and manually verified.

Small molecules

Palbociclib and PF3600 were obtained directly from Pfizer and were dissolved in anhydrous DMSO (Sigma-Aldrich, Cat# 276855); Palbociclib was added to a final concentration of 100 nM or 1μM and PF3600 was added to a final concentration of 25 nM, 100 nM, or 500 nM as indicated. RO3306 was purchased from SelleckChem (Cat# S7747). CVT-313 was purchased from EMD Millipore (Cat# 238803), dissolved in anhydrous DMSO, and used at a final concentration of 60 μM[4]. Abemacicib (Cat# HY-16297A), Ribociclib (Cat# HY-15777) and Fadraciclib (Cat# HY-101212) were purchased from MedChemExpress and dissolved in anhydrous DMSO. Abemaciclib was added to a final concentration of 1μM, Ribociclib was added to a final concentration of 5μM, and Fadraciclib was added to a final concentration of 600 nM. 3MB-PP1 (Cayman Chemical, Cat# 17860) was dissolved in anhydrous DMSO and was added to a final concentration of 10 μM. Indole-3-acetic acid (Sigma-Aldrich, Cat# I5148) was dissolved in sterile water and was added to a final concentration of 250 μM. Doxycycline (Sigma-Aldrich, Cat# D9891) was dissolved in sterile water and was added to a final concentration of 500 ng/mL. Pan-E2F inhibitor was purchased from Sigma-Aldrich (Cat# 324461), dissolved in DMSO at a stock concentration of 25 mM, and used at a final concentration of 50 μM.[49] This inhibitor may have off-target effects at this concentration, but this is the only commercially available E2F inhibitor. Commercial PF-07104091 was purchased from ChemiTek (Cat# CT-PF0710, Lot #01, >99% purity) and dissolved in DMSO at a stock concentration of 10 mM.

Phospho-serine 807/811 Rb and phospho-threonine 84 NCL ELISA

MCF10A or MCF7 cells were seeded at 25,000 cells/well in growth media in 96-well cell culture plates and allowed to adhere at 37°C with 5% CO_2 overnight. The following day, compounds were serially diluted from 10 mM stock for 11-point 3-fold dilution curve in DMSO (Sigma). Compounds were intermediately diluted 1:200 into growth media prior to diluting 1:5 on cells for final concentration 10 μM top dose in 0.1% DMSO on cells. Cells were treated for either 1 h or 24 h at 37°C in 5% CO_2. Cells were lysed in lysis buffer (Cell Signaling Technologies, 9803) containing protease inhibitor cocktail (Cell Signaling Technologies, 5872), SDS, and PMSF on ice and transferred to ELISA plates pre-coated with either anti-phospho-Ser807/811 Rb or anti-total NCL for overnight incubation at 4°C. Plates were washed with phosphate buffered saline to remove residual unbound cellular proteins and total Rb detection antibody (Cell Signaling Technologies, 9309) or anti-phospho-Ser84 NCL antibody was added for 90 min at 37°C. Following washing to remove unbound antibody, HRP-tagged antibody (Cell Signaling Technologies, 7076 or 7074) was allowed to bind for 30 min at 37°C. Following washing to remove unbound HRP antibody, Glo Substrate Reagent (R&D Systems, DY993) was added and incubated protected from light for 5–10 min. Plates were read in luminescent mode on an Envision plate reader (Perkin Elmer) and IC50 values calculated using GraphPad Prism Version 8.0.2.

Western blotting

Lysates were prepared using diluted 4X LDS sample buffer (ThermoFisher NP007) using equal numbers of cells. Proteins were separated using NuPAGE precast polyacrylamide gels (ThermoFisher NP0301). Primary antibodies used are specified in the key resources table. HRP-conjugated antibodies were used for visualization.

For western blots in Figure 7, protein extraction was performed in protein lysis buffer (50 mM Tris-HCl pH 7.4, 150 mM NaCl, 0.5% NP-40) supplemented with a cocktail of protease and phosphatase inhibitors (cOmplete Mini, Roche, 11836153001; Phosphatase Inhibitor Cocktail 2 and 3, Sigma, P5726 and P0044). Protein concentrations were measured using Bradford (Bio-Rad) method. 25 g of protein extracts obtained from tumor tissue were separated on NUPAGE TM 4–12% Bis-Tris Midi gels (Invitrogen), transferred

to a nitrocellulose membrane (GE Healthcare) and blotted with primary antibodies. Primary antibodies were detected with goat secondary antibodies directed against mouse or rabbit IgGs and visualized with ECL Western Blot detection solution (GE Healthcare).

Immunoprecipitation

MCF10A cells were grown to ~70% confluency and treated with 100nM PF3600 for 0, 4, or 12 h. Cells were lysed with MSD Lysis Buffer (MSD R60TX-2) supplemented with a protease inhibitor cocktail (Roche 05 892 970 001) and 1mM Na_3VO_4. Soluble protein concentration was determined via bicinchoninic acid protein assay (BCA; Pierce 23227). 1000μg total soluble protein was incubated with 4μg of mouse α-CDK2 antibody (sc-6248), in 900μL total lysis buffer (12 h). 100μL of 50% slurry Protein A/G Agarose (Pierce 20421) was added to each pulldown and incubated (12 h). The resin was washed and centrifuged 3 times and excess supernatant was removed. Western blots were performed as described above against CDK2 (sc-6248 for IP, ab32147 for blotting), CDK1 (ab133327), Cyclin A2 (sc-751 for blotting CDK2 IP; sc-271682 for blotting CDK1 IP), and Cyclin E1 (ab33911).

mRNA FISH

Cells were seeded on a glass-bottom 96-well plate coated with collagen 24 h prior to drug treatment. Cells were fixed with 4% paraformaldehyde and were processed for RNA-FISH analysis using the ViewRNA ISH Cell Assay Kit (Thermo Fisher, #QVC0001). mRNA probes were hybridized for 3 h, followed by 30 min probe pre-amplification, 30 min probe amplification, and 30 min fluorescent labeling. All hybridization, amplification, and labeling steps were performed in a humidified incubation chamber at 40 °C. Probes used in this study are listed in the key resources table. Blocking and immunofluorescence staining were performed after FISH labeling.

Phosphoproteomics

Phospho-peptide enrichment was performed by TiO2.[80] Briefly, a 4:1 ratio of titanium dioxide beads: digested peptides was used to enrich phospho-peptides in a lactic acid buffered system. Enriched peptides were desalted with C18 reverse phase desalting columns and lyophilized to dryness. Dried peptides were stored at −80°C until labeling. TMT-labeled peptides were reverse phase basic pH fractionated into 96 fractions that were concatenated to 24.[80–82] Briefly, samples were separated on a 4.6 mm × 250 mm C18 column on a Vanquish Flex HPLC. Separation was performed across a linear gradient of 8–28% (60 min) acetonitrile in 10mM ammonium bicarbonate with a flow rate of 0.5 mL/min. Fractions were lyophilized and stored at 80°C until MS analysis. For LC-MS2/MS3 analysis, samples were reconstituted in 10 μL of 5% acetonitrile in 5% formic acid and 8 μL of each fraction was injected on the Orbitrap Fusion Lumos for analysis.

Peptides were eluted on a 165-min gradient of 7–32% solvent B (80% acetonitrile in 0.1% formic acid) at 300 nL/min on a PepMap RSLC C18 column (2 μm, 100 Å, 75 μm × 50 cm) heated to 60°C. Spectra were acquired in Top Speed mode, with a 5 s cycle. MS1 data were collected in the Orbitrap at 60000 resolution across a range of 500–1500 *m/z*. An automatic gain control (AGC) target of $2x10^5$ was used with a maximum injection time of 100 ms. MS2 data were acquired in the ion trap with a rapid scan rate, maximum injection time of 70 ms, and an AGC target of $2x10^4$. The quadrupole was used for isolation, with an isolation window of 0.5 *m/z*. Peptides were fragmented with CID at 30% normalized collision energy with an activation time of 10 ms and an activation Q of 0.25. For MS3 spectra, up to 10 ions were selected for synchronous precursor selection, and data were collected at 60000 resolution in the Orbitrap. Ions were fragmented with HCD at an energy of 55%. MS3 AGC was set to $1x10^5$ with a maximum injection time of 250 ms and a first mass of 110 *m/z*. Data at all stages were centroided.

Resultant raw files were processed on an IP2GPU server (Integrated Proteomics Applications, Inc.). Data were searched with the ProLuCID algorithm[83] against the Uniprot Human Database (Downloaded January 29, 2018) concatenated with the current contaminants database and reverse database. Carbamidomethylation of Cysteine residues (+57.02146) and TMT-11 modification of peptide n-termini and Lysine residues (+229.162932) were included as static modifications. Oxidation of Methionine (+15.9949) and phosphorylation of Serine, Threonine, and Tyrosine (+79.966331) were included as variable modifications. A maximum of 4 variable modifications and two missed cleavages were allowed. Peptides had to have a minimum length of 6 amino acids to be considered. Data were searched with a 50 ppm MS1 tolerance[84] and 800 ppm MS2 tolerance. Final data were filtered to a 1% protein level false discovery rate.

Data were normalized in a multistep process. First, data were normalized to a pooled bridge channel to account for run-to-run instrument performance differences and then median-scrubbed to account for any mixing errors.[80] All phospho data were processed and analyzed at the peptide level.

QUANTIFICATION AND STATISTICAL ANALYSIS

Cell tracking and single-cell CDK2 activity analysis

Cell tracking was performed using published MATLAB scripts.[78] The tracking code is available for download at https://github.com/scappell/Cell_tracking. Cell counts over time were obtained by counting the number of segmented nuclei in each frame of the movie.

Asynchronously cycling cells that divided and received drug treatments during the imaging period were initially segmented into categories based on the cells' time of mitosis relative to the time of drug addition.[85] These cells were then additionally subcategorized

based on their DHB cytoplasmic/nuclear (C/N) ratio after the mitotic event. C/N ratio was calculated by quantifying the ratio of cytoplasmic to nuclear mean DHB fluorescence, with the cytoplasmic component calculated as the mean of the top 50th percentile of a ring of pixels outside of the nuclear mask.

Cells were classified as $CDK2^{inc}$ if the DHB C/N ratio was above 0.5 units 3 h after anaphase, otherwise they were classified as $CDK2^{low}$. $CDK2^{inc}$ cells are plotted throughout except for Figure S3A-S3D where all cells were plotted. The median of the single-cell traces in a subcategory was then used to create a median trace with 95% confidence interval representative of the particular subcategory. All cell trace analysis was performed using MATLAB scripts (see key resources table).

Statistics

For all time-lapse imaging quantifications where the median DHB cytoplasmic/nuclear (C/N) ratio is plotted, 95% confidence intervals are shown for every time point as shaded bands, where non-overlapping shading between treatment groups indicates a statistically significant difference with a p value < 0.05. Validation of this visualization of statistical significance is shown in Figure S1A.

Significance levels for unpaired t-tests are reported as p value summaries on indicated bar charts < 0.05 (*), < 0.01 (**), < 0.001 (***) and < 0.0001 (****) with corresponding star notations. Throughout the manuscript, 'ns' denotes no statistical significance.

All data shown are representative of multiple experiments. See Table S1 for statistics on sample sizes and independent experimental repeats.

Supplemental figures

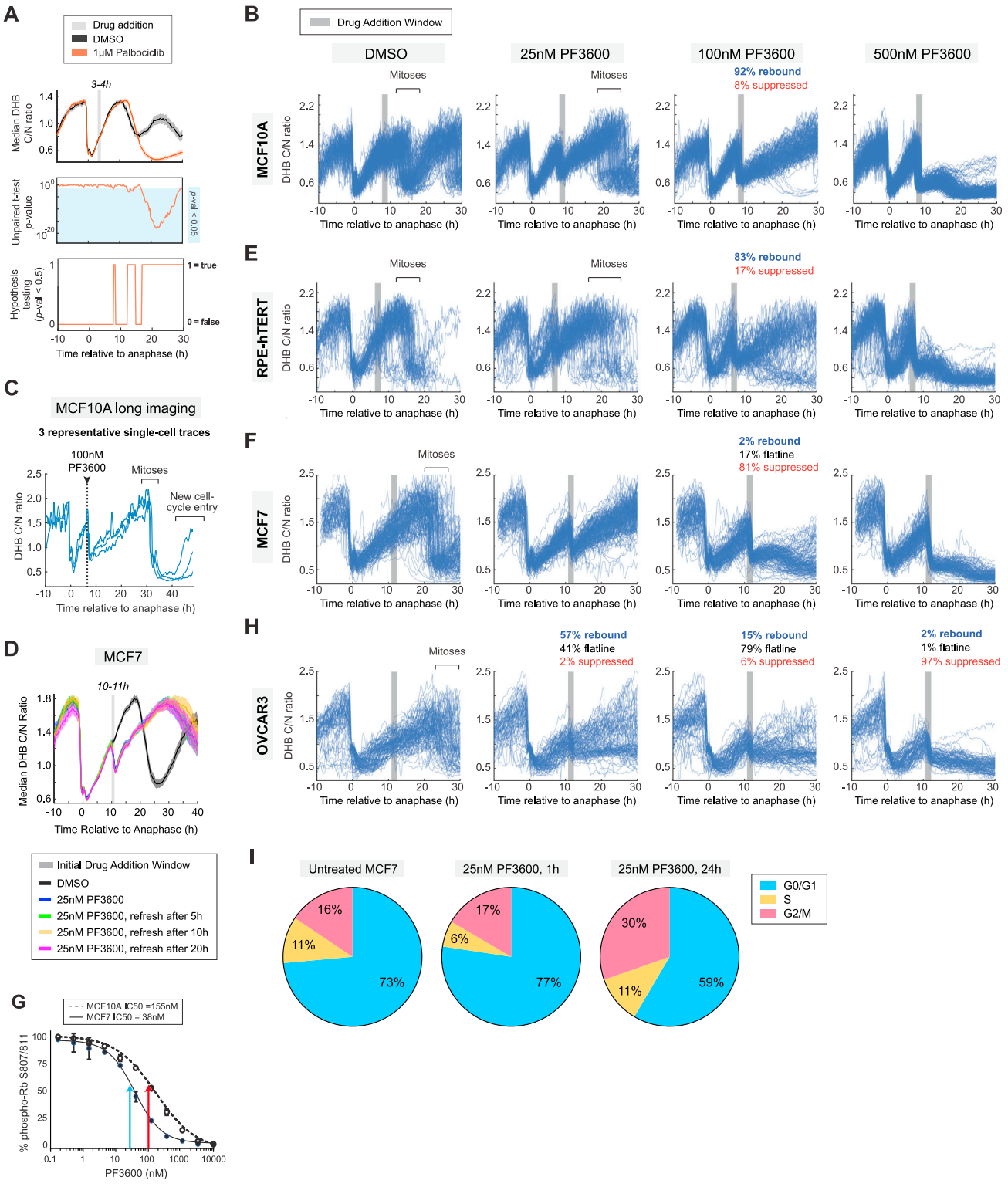

(legend on next page)

Figure S1. CDK2 activity is acutely inhibited by low-dose PF3600, but phosphorylation rebounds rapidly, related to Figure 1

(A) Validation of 95% confidence interval band plotting. Time-lapse plot of median DHB C/N ratio with 95% confidence interval bands for DMSO- and Palbociclib-treated cells is replicated from Figure 1C to use as an example (top). Corresponding p values are calculated for 100 sampled cells within each condition (middle), and true-false results from hypothesis testing are plotted based on whether the p value is less than 0.05 at each time point (bottom).

(B, E, F, and H) DHB C/N single-cell traces for the individual MCF10A, RPE-hTERT, MCF7, and OVCAR3 cells plotted in Figures 1F, 1H–1J. Any additional mitoses after drug treatment are labeled.

(C) Representative DHB C/N single-cell traces from MCF10A tracked over 50 h to view delay in mitosis in presence of 100nM PF3600.

(D) DHB sensor phosphorylation in MCF7 treated with 25 nM PF3600. Drug was refreshed 5, 10 and 20 h after initial PF3600 addition to test whether the rebound in DHB was due to drug degradation or efflux.

(G) MCF10A and MCF7 cells were treated with increasing doses of PF3600 for 1 h, and phospho-Rb (S807/811) was measured by ELISA. Mean of 2 technical replicates plotted ± SD.

(I) Cell-cycle distribution of MCF7 cells treated with DMSO or 25 nM PF3600 for timepoints matched to those used in the phosphoproteomics. Cells were stained with Hoechst and EdU to deduce cell-cycle phases: G0/G1 (2N DNA content and EdU^{-}), S (EdU^{+}), and G2/M (4N DNA content and EdU^{-}).

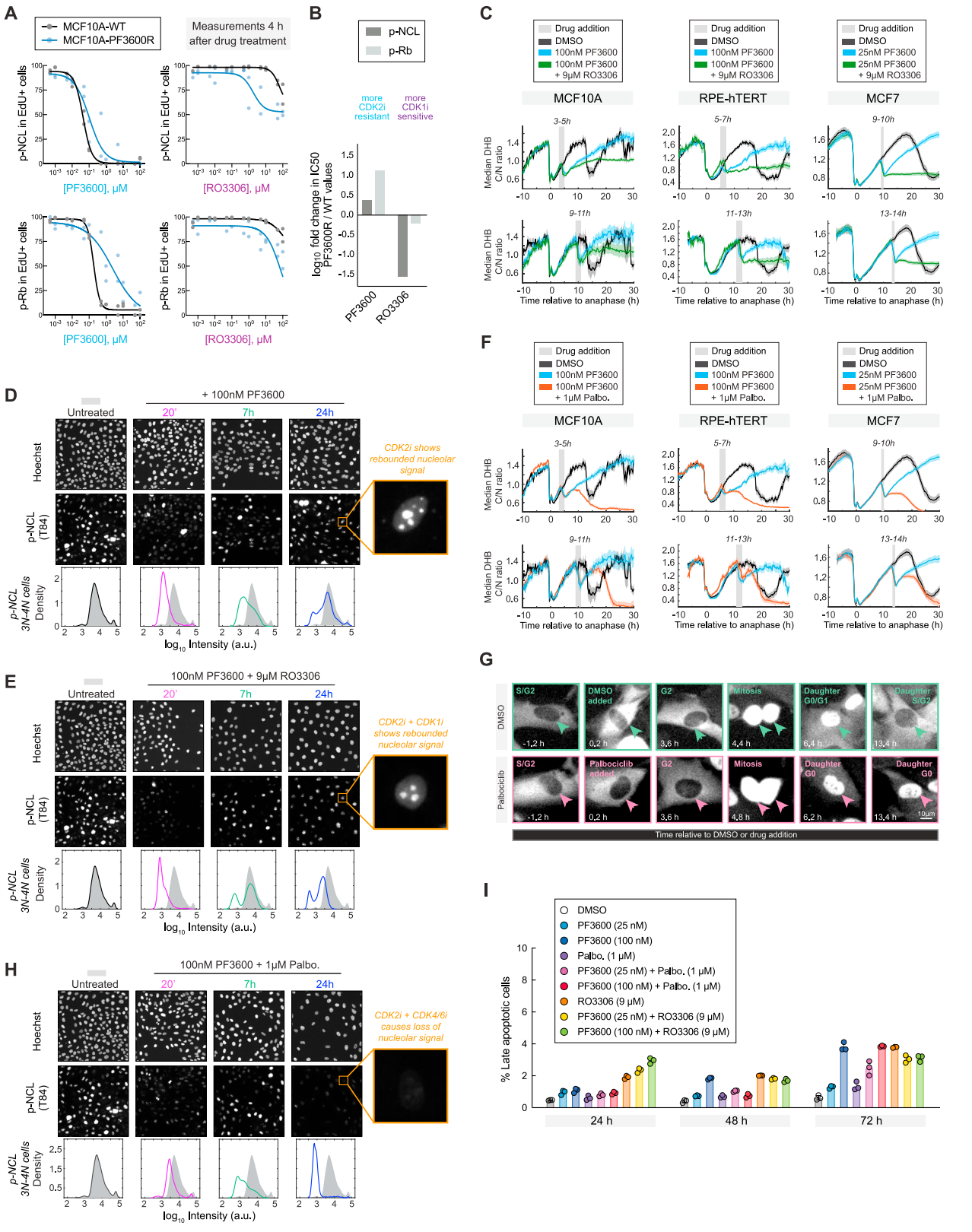

(legend on next page)

Figure S2. Co-inhibition of CDK2 and CDK4/6 blocks the rebound in CDK2 activity, related to Figure 2

(A) MCF10A were treated continuously with 100 nM PF3600 for 1 month to generate resistant MCF10A-PF3600R cells. Without any drug holiday, MCF10A-WT and MCF10A-PF3600R were then treated with the indicated dose curves of PF3600 or RO3306 for 4 h after which cells were fixed and processed for immunofluorescence. Dose-response curves showing the percent of phospho-NCL$^+$ or phospho-Rb$^+$ cells among EdU$^+$ cells were plotted. At least 2 technical replicates per condition, each individual replicate shown. Four-parameter inhibitory Hill equation was employed in GraphPad Prism to fit the curves.

(B) IC50 values from dose-response curves show the change in PF3600 and RO3306 sensitivities for the MCF10A-PF3600R cell line.

(C) Additional time slices from the experiment in Figure 2A showing DHB sensor phosphorylation in MCF10A, RPE-hTERT, and MCF7 cells treated with the drugs indicated. For MCF10A and RPE-hTERT, 100 nM PF3600 was used; for MCF7, 25 nM PF3600 was used.

(D) MCF10A cells were treated with 100 nM PF3600 for the indicated times, and fixed and stained for phospho-Nucleolin. Hoechst was used to quantify DNA content. Mean nuclear signals were quantified for cells with 3-4N DNA content and plotted as probability density histograms. The histogram representing the phospho-NCL distribution in untreated cells is propagated to the other time points as a gray shaded region.

(E) MCF10A cells were treated with 100 nM PF3600 + 9 μM RO3306 for the indicated times, and fixed and stained for phospho-Nucleolin. Mean nuclear signal was quantified for cells with 3-4N DNA content and plotted as probability density histograms. The gray histograms represent the phospho-NCL distribution in untreated cells; untreated images and gray histograms are reproduced from (D).

(F) Additional time slices from the experiment in Figure 2B showing DHB sensor phosphorylation in MCF10A, RPE-hTERT, and MCF7 cells treated with the indicated drugs. For MCF10A and RPE-hTERT, 100 nM PF3600 was used; for MCF7, 25 nM PF3600 was used.

(G) Representative images of the CDK2 sensor over time in RPE-hTERT cells treated with DMSO or Palbociclib, from the experiment in Figure 2C. These treatments have no effect on sensor phosphorylation, as cells continue through their ongoing cell cycle at normal pace and complete mitosis. The DMSO-treated daughter cell progresses through a new cell cycle, whereas the Palbociclib-treated daughter cell enters a prolonged G0 state.

(H) MCF10A cells were treated with 100 nM PF3600 + 1 μM Palbociclib for the indicated times, and fixed and stained for phospho-Nucleolin. Image contrast settings across panels (D), (E) and (H) are the same. Mean nuclear signal was quantified for cells with 3-4N DNA content and plotted as probability density histograms. The gray histograms represent the phospho-NCL distribution in untreated cells; untreated images and histograms are reproduced from (D).

(I) Percent apoptotic cells after the indicated time and drug treatments, as determined by flow cytometry of MCF10A cell suspensions stained for propidium iodide and Annexin V. Bars show mean ± SD.

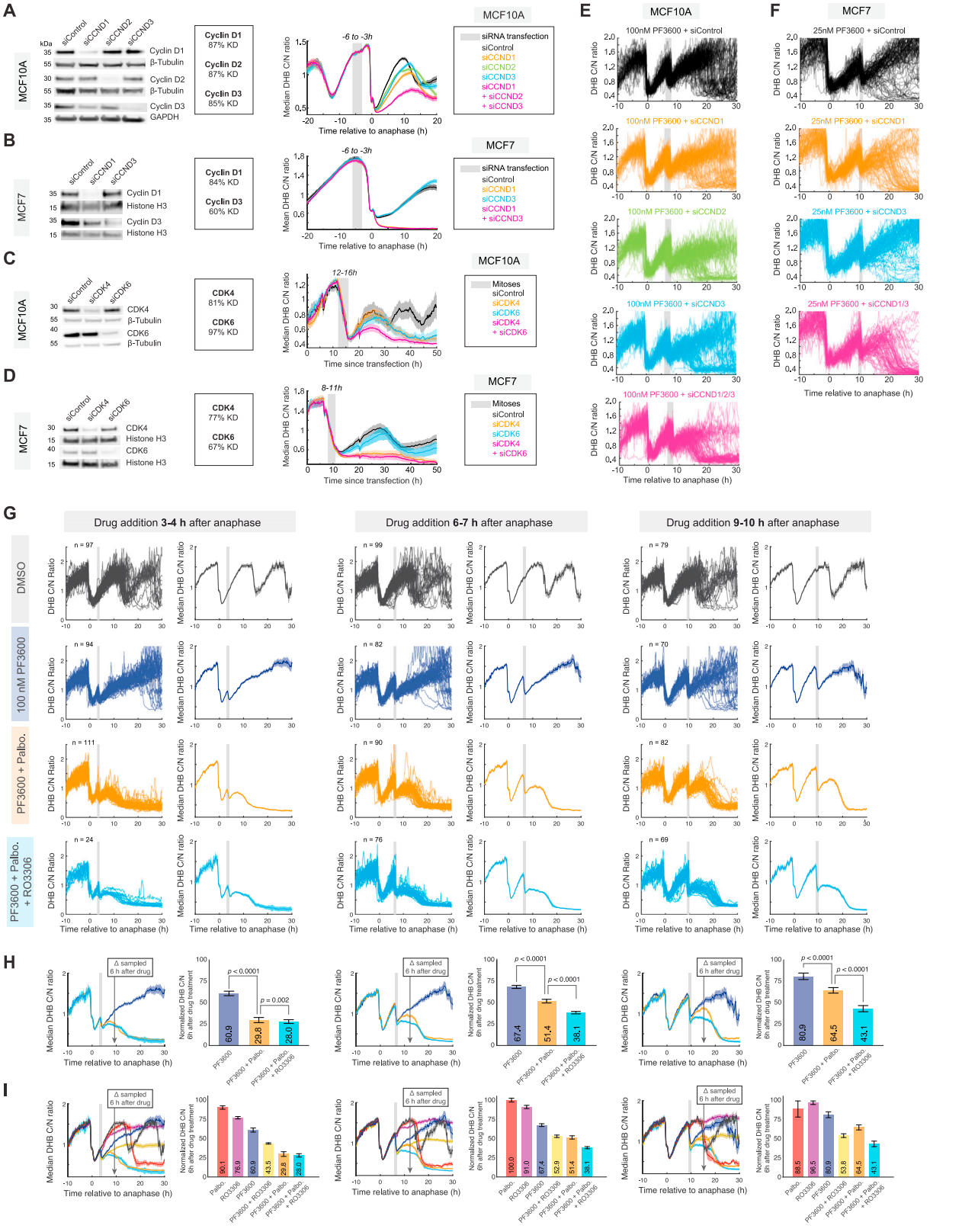

(legend on next page)

Figure S3. CDK4/6-cyclin D drives the rapid rebound upon CDK2 inhibition, related to Figure 3

(A and B) Left: Western blots validating depletion of indicated cyclins in MCF10A and MCF7 24 h after siRNA transfection. β-tubulin, GAPDH, or Histone H3 are used as a loading control. Right: DHB sensor phosphorylation in MCF10A or MCF7 cells after treatment with the indicated siRNAs. As MCF7 cells do not express cyclin D2,[86] CCND2 knockdown was omitted from the MCF7 experiment. Data are plotted as median DHB C/N ratio with 95% confidence interval for all cells receiving siRNA transfection mix 3–6 h prior to anaphase, as marked by the gray bar. The orange curve for siCCND1 in MCF7 cells falls behind the magenta curve for siCCND1/D3 and thus is not visible.

(C and D) Left: Western blots validating the depletion of CDK4 and CDK6 in MCF10A and MCF7 24 h after the indicated siRNA treatment. β-tubulin or Histone H3 are used as a loading control. Right: DHB sensor phosphorylation in MCF10A or MCF7 cells after treatment with the indicated siRNAs. Cells were imaged for 50 h starting immediately following siRNA transfection. x axis represents time since transfection. Data are plotted as median DHB C/N ratio with 95% confidence interval for all cells undergoing mitosis *n* h after the time of transfection, where *n* is indicated on the plot as a vertical gray bar.

(E and F) Single-cell DHB C/N traces for the individual MCF10A (E) and MCF7 (F) cells plotted in Figures 3A and 3B.

(G) DHB sensor phosphorylation in MCF10A cells after indicated CDKi monotherapies and combinations in early (3–4 h), mid (6–7 h), and late (9–10 h) drug addition windows. Single-cell traces and corresponding median plots are displayed.

(H–I) Left: DHB sensor phosphorylation in MCF10A cells after indicated treatment combinations of 100 μM PF3600, 1 μM Palbociclib or 9 μM RO3306. 6 h after the drug addition window, the DHB C/N ratio was sampled to assess hump magnitude. Right: Bar plot of normalized DHB signal, where 100% represents the maximum DHB signal reached in an unperturbed cell cycle and 0% represents the floor of the DHB signal (achieved in the triple drug setting). Median value of all cells ± 95% CI.

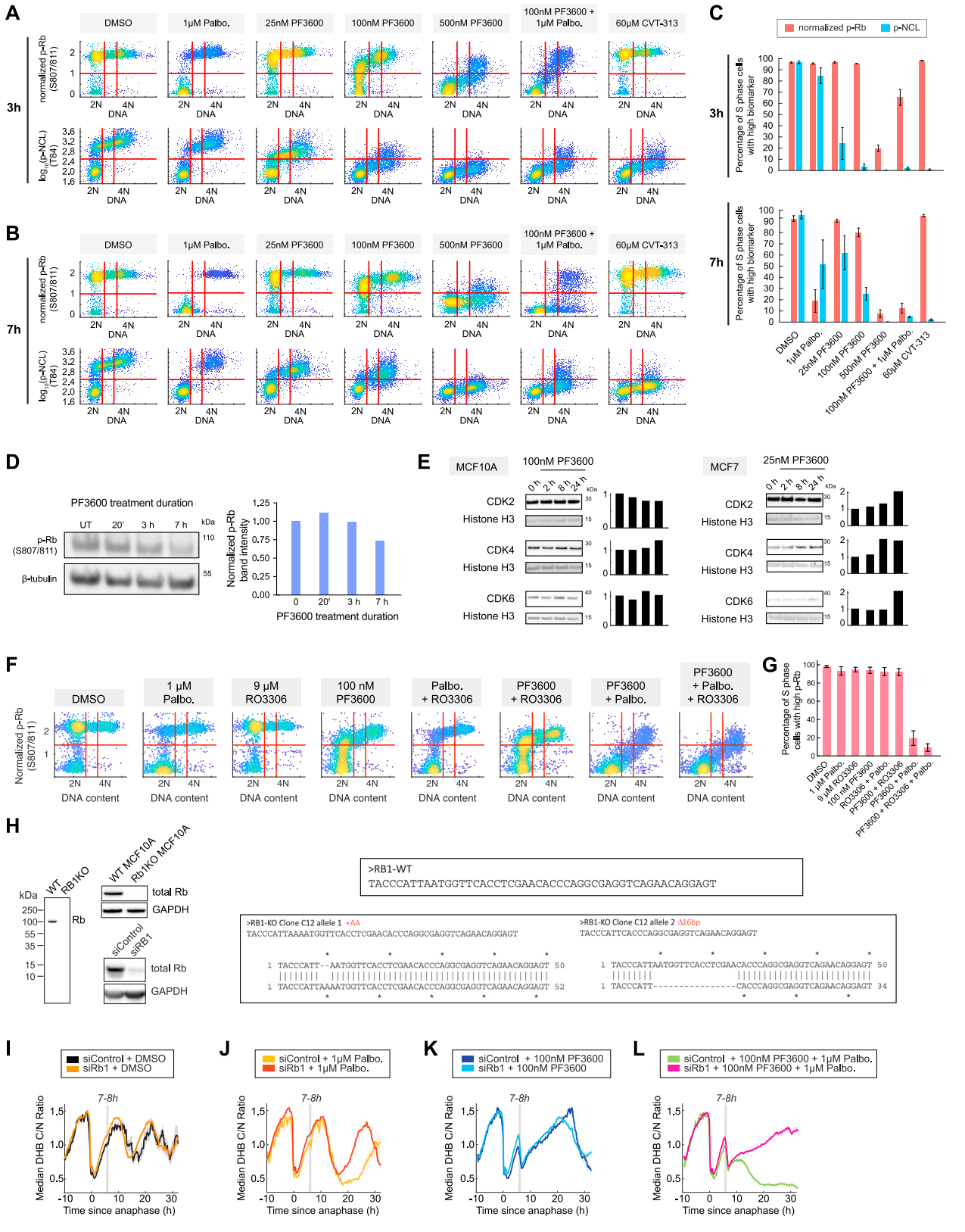

(legend on next page)

Figure S4. The CDK2 rebound upon low-dose PF3600 treatment depends on Rb1 status, related to Figure 4

(A and B) Density scatterplots portraying the effect of the indicated compound on normalized phospho-Rb or phospho-NCL in MCF10A after 3 h (A) or 7 h (B). DMSO plots are reproduced from Figure 4C; red lines as in Figures 4A and 4B.

(C) Bar charts quantifying the fraction of S phase cells with high levels of the indicated biomarker after 3 or 7 h of the indicated treatments. Data for DMSO are reproduced from Figure 4A and B. Mean of 4 technical replicates plotted ± SD.

(D) Western blot and quantification of phospho-Rb (S807/811) in MCF10A treated with PF3600 as indicated. β-actin is used as a loading control.

(E) Western blot and quantification of CDK2, CDK4, or CDK6 in MCF10A and MCF7 treated with PF3600 as indicated. Histone H3 is used as a loading control.

(F) Density scatterplots portraying the effect of the indicated compound(s) on phospho-Rb in MCF10A after 20 min of drug treatment. Red vertical lines indicate gating based on Hoechst stain for subsequent quantification of the S phase population; red horizontal line was set at the midpoint between the high and low populations of normalized phospho-Rb (S807/811) in 2N cells.

(G) Percent of S phase cells from (F) with high levels of phospho-Rb after 20 min of drug treatment. Mean of 4 technical replicates plotted ± SD.

(H) Left: Western blot validation of Rb1 knockout and Rb1 knockdown in MCF10A. Full-length western blot of Rb1 KO cells shows a complete knockout of Rb1 and that no truncated Rb1 proteins remain. GAPDH was used as a loading control. Right: Sequence validation of RB1 KO clone C12.

(I–L) DHB sensor phosphorylation in MCF10A electroporated with nontargeting siRNA (siControl) or siRNA targeting Rb1 40 h before treatment with the indicated drugs.

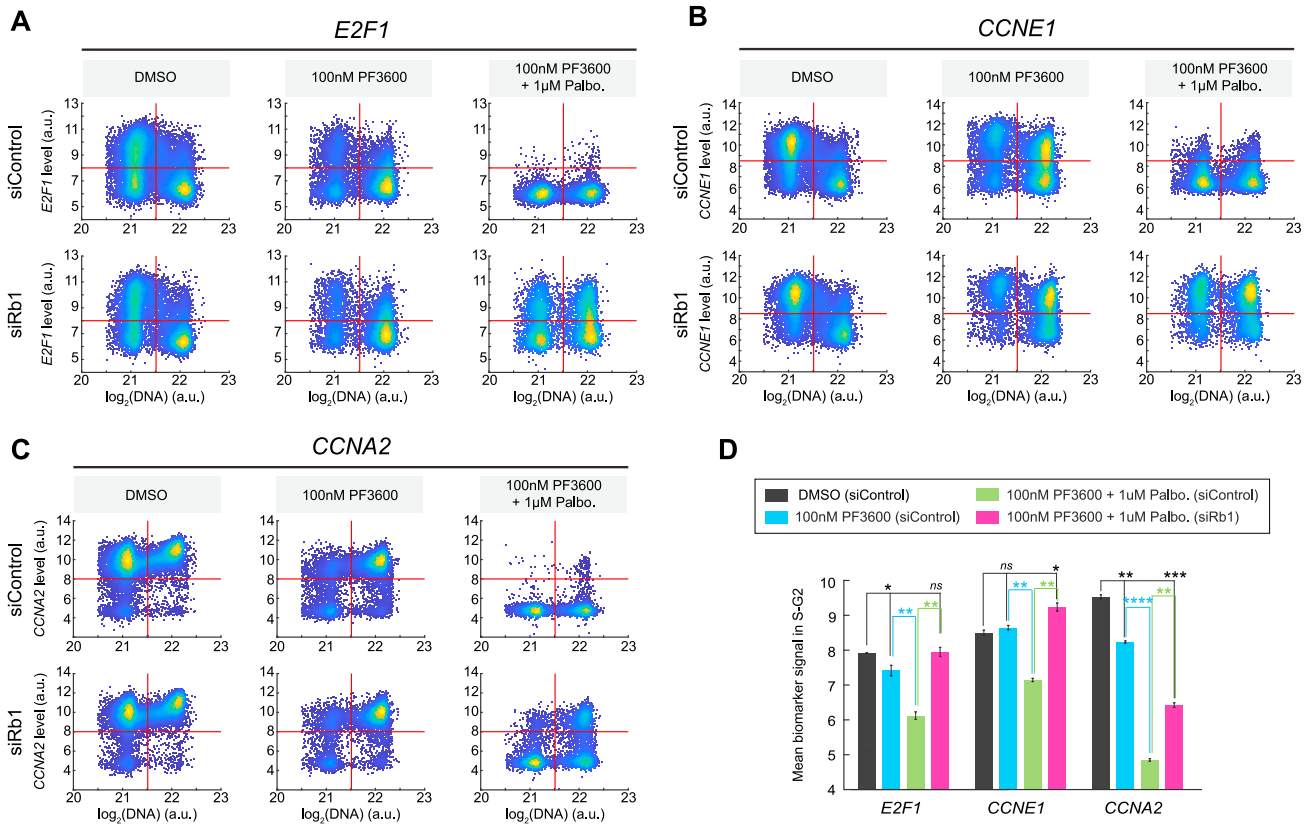

Figure S5. Rb1 status determines cyclin E and A expression in the response to CDK2 inhibition, related to Figure 5

(A–C) Density scatterplots of median cytoplasmic RNA FISH signal of *E2F1*, *CCNE1*, *CCNA2* plotted against DNA content in cells subjected to nontargeting siRNA (*top*) or siRNA against Rb1 (*bottom*). Red lines indicate gates used to quantify the 'S-G2 high' biomarker population in the top-right quadrant. Cells were treated with the indicated drugs for 14 h.

(D) Bar chart quantifying the mean signal in S-G2 cells for the indicated mRNA plotted in (A) through (C). Asterisks correspond to unpaired t tests between the indicated conditions. Mean of 2 technical replicates plotted ± SD.

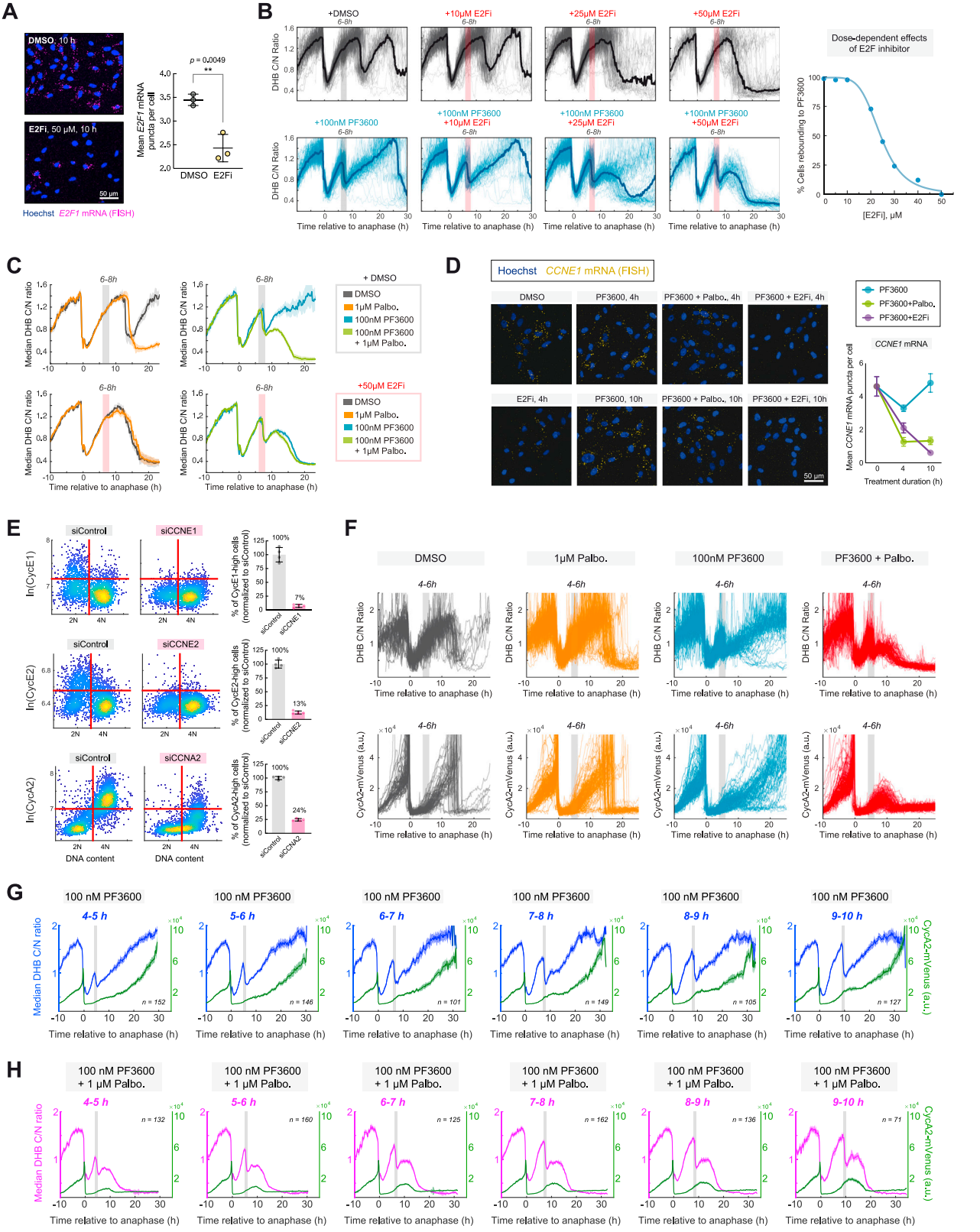

(legend on next page)

Figure S6. The CDK-Rb1-E2F axis drives cyclin A2 expression to support sustained adaptation to low-dose PF3600, related to Figure 6

(A) Representative images of MCF10A treated with E2Fi for 10 h and stained for *E2F1* mRNA (left). Quantification of *E2F1* mRNA (right). Mean of 3 replicates plotted ± SD.

(B) Left: DHB C/N single-cell traces for MCF10A cells treated with indicated doses of E2Fi with or without 100 nM PF3600. The median value is plotted on top of single-cell traces as a thick dark line. In PF3600-treated cells, increasing doses of E2Fi lead to fewer cells with a rebound in CDK2 activity. Right: Quantification of the percent of cells with rebounding CDK2 activity as a function of E2Fi dose.

(C) DHB sensor phosphorylation in MCF10A treated with the indicated drugs (gray or pink bar). E2Fi (bottom) was added at the same time as PF3600 and Palbociclib.

(D) Representative images of MCF10A treated with the indicated drug for 4 h or 10 h and stained for *CCNE1* mRNA (left). Quantification of the *CCNE1* mRNA (right). Mean of 3 replicates plotted ± SD.

(E) Knockdown validation of cyclins E1, E2, and A2 after 6 h of siRNA treatments in MCF10A cells by immunofluorescence. Cells were co-stained and gated for phospho-Rb^{+} status, to assess knockdown efficiency in actively cycling cells. For cyclins E1 and E2, 2N cells were selected for quantification in the corresponding bar chart. For cyclin A2, 4N cells were selected for quantification in the corresponding bar chart. Mean of 3 replicates plotted ± SD.

(F) DHB C/N single-cell traces for the RPE-hTERT CycA2-mVenus cells plotted in Figure 6H.

(G–H) Overlay of DHB sensor phosphorylation and endogenous cyclin A2-mVenus intensity in RPE-hTERT cells treated at varying times across the cell cycle (gray bars) with low-dose PF3600 (G) or low-dose PF3600 plus Palbociclib (H).

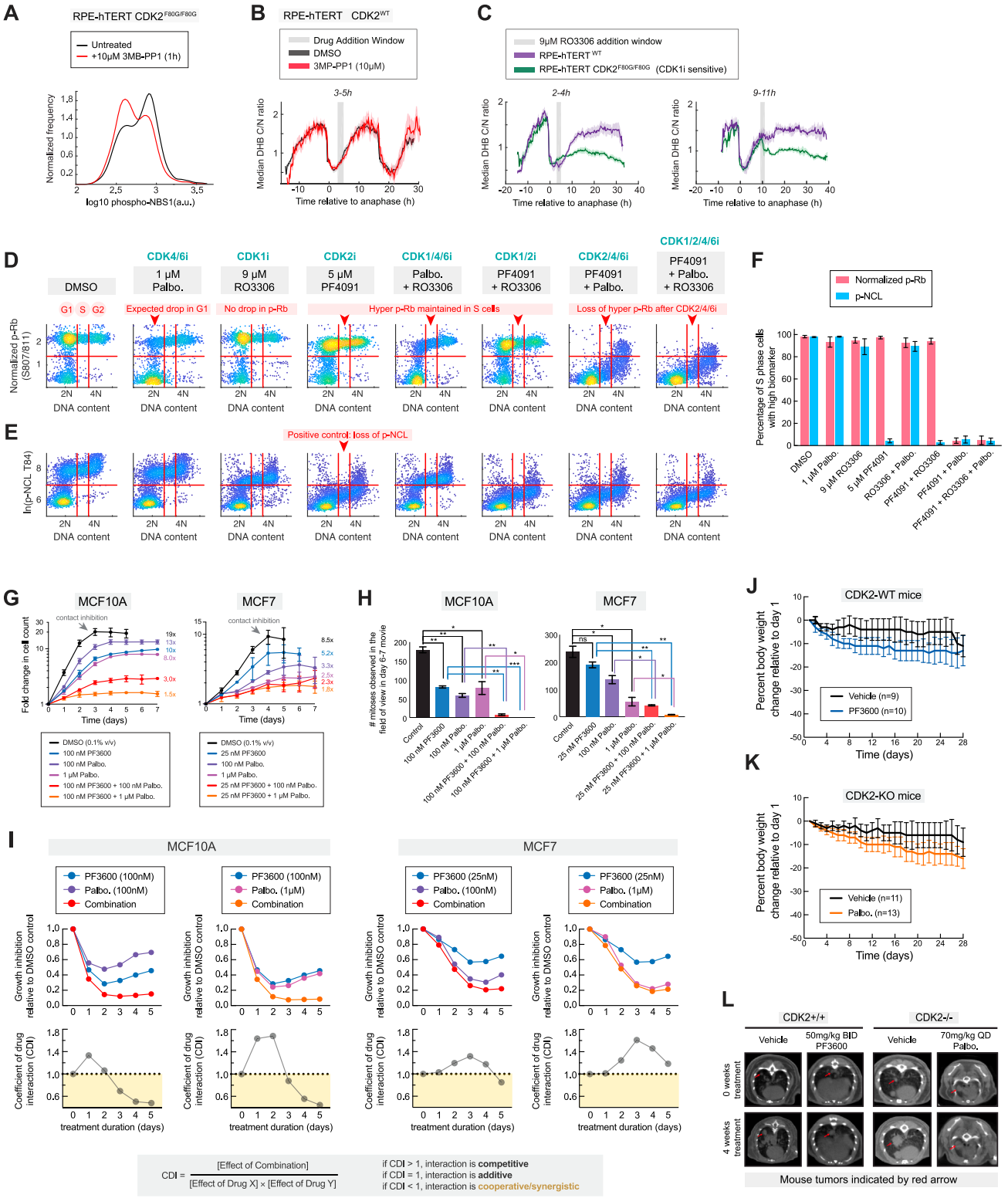

Figure S7. Orthogonal CDK2 inhibition approaches and *in vivo* studies indicate that cell-cycle progression is maintained by the combined sum of CDK2/4/6 activity, related to Figure 7

(A) RPE-hTERT CDK2$^{F80G/F80G}$ treated with 10 μM 3MB-PP1 for 1 h and fixed and stained with phospho-NBS1 antibody to validate the inhibition of CDK2 using 3MB-PP1. Probability density histogram of nuclear phospho-NBS1 signal is shown. Mean of two technical replicates plotted.

(legend continued on next page)

(B and C) DHB sensor phosphorylation in the indicated RPE-hTERT cell lines with the indicated drugs. Inhibition of CDK1 using RO3306 leads to a much greater drop in DHB phosphorylation in RPE-hTERT CDK2$^{F80G/F80G}$ cells as compared to wild-type cells. Furthermore, in RPE-hTERT CDK2$^{F80G/F80G}$ cells, CDK1 is active unusually early in the cell cycle, as revealed by a plateauing DHB signal and lack of cell-cycle progression when RO3306 is added 2–4 h after anaphase (C, left). We conclude that the DHB sensor responds primarily to CDK2 activity in contexts where CDK2 is fully functional, but that CDK1 contributes to phosphorylation of CDK2 substrates in the RPE-hTERT CDK2$^{F80G/F80G}$ genetic background where CDK2 is not fully functional, thereby muting the inhibition of DHB phosphorylation attainable with 3MB-PP1 in Figure 7A.

(D and E) Density scatterplots portraying the effect of the indicated compound on normalized phospho-Rb (D) or phospho-NCL (E) in MCF10A after 20 min.

(F) Bar charts quantifying the fraction of S phase cells with high levels of the indicated biomarker after 20 min of indicated treatments from (D) and (E). Mean of 4 technical replicates plotted ± SD.

(G) Wells containing MCF10A or MCF7 cells were imaged daily for 7 days following the indicated treatments to assess proliferation by automated counting of nuclei using H2B-mTurquoise. Unfettered proliferation led to contact inhibition in the DMSO control by day 3 (MCF10A) or day 4 (MCF7). Points indicate mean of at least 3 technical replicates ± SD.

(H) MCF10A or MCF7 cells from (G) were subject to time-lapse imaging over 24 h from day 6 to 7 of the indicated treatment to track the number of mitoses. Fresh control cells were seeded at low density 24 h before the imaging period. Error bars indicate mean number of mitoses observed ± SD of two movies. Note that localized regions of contact inhibition caused a reduced rate of mitosis in MCF10A treated with 100 nM Palbociclib. Asterisks correspond to unpaired t-tests between the indicated conditions.

(I) Growth inhibition and coefficient of drug interaction analysis (CDI) probing for cooperativity between Palbociclib and PF3600 in (G).

(J–K) Normalized body weight changes in treated mice. Sample sizes of mouse cohorts indicated on plots. Mean ± 95% CI.

(L) Representative CT scans of each cohort of mice from Figure 7I, upon tumor detection (top) and after four weeks of the indicated treatment (bottom). Red arrows point to the tumor.